Safe Autonomy for Uncrewed Surface Vehicles Using Adaptive Control and Reachability Analysis

Karan Mahesh*

Aurora Flight Sciences, a Boeing Company Cambridge, MA, USA

mahesh.karan@aurora.aero

Tyler M. Paine*†

Marine Autonomy Laboratory
Massachusetts Institute of Tech.
Cambridge, MA, USA.
Woods Hole Oceanographic Institution
Woods Hole, MA, USA

tpaine@mit.edu

Max L. Greene

Aurora Flight Sciences, a Boeing Company Cambridge, MA, USA

greene.max@aurora.aero

Nicholas Rober

Aerospace Controls Laboratory
Massachusetts Institute of Technology
Cambridge, MA, USA.

nrober@mit.edu

Steven Lee

Aurora Flight Sciences, a Boeing Company Cambridge, MA, USA

lee.steven@aurora.aero

Sildomar T. Monteiro

Aurora Flight Sciences, a Boeing Company Cambridge, MA, USA

monteiro.sildomar@aurora.aero

Anuradha Annaswamy

Active-Adaptive Control Lab Massachusetts Institute of Tech. Cambridge, MA, USA.

aanna@mit.edu

Michael R. Benjamin

Marine Autonomy Lab Massachusetts Institute of Tech. Cambridge, MA, USA.

mikerb@mit.edu

Jonathan P. How

Aerospace Controls Lab Massachusetts Institute of Tech. Cambridge, MA, USA.

jhow@mit.edu

Abstract

Marine robots must maintain precise control and ensure safety during tasks like ocean monitoring, even when encountering unpredictable disturbances that affect performance. Designing algorithms for uncrewed surface vehicles (USVs) requires accounting for these disturbances to control the vehicle and ensure it avoids obstacles. While adaptive control has addressed USV control challenges, real-world applications are limited, and certifying USV safety amidst unexpected disturbances remains difficult. To tackle control issues, we employ a model reference adaptive controller (MRAC) to stabilize the USV along a desired trajectory. For safety certification, we developed a reachability module with a moving horizon estimator (MHE) to estimate disturbances affecting the USV. This estimate is propagated through a forward reachable set calculation, predicting future states and enabling real-time safety certification. We tested our safe autonomy pipeline on a Clearpath Heron USV in the Charles River, near MIT. Our experiments demonstrated that the USV's MRAC controller and reachability module could adapt to disturbances like thruster failures and drag forces. The MRAC controller outperformed a PID baseline, showing a 45%-81% reduction in RMSE position error. Additionally, the reachability module provided real-time safety certification, ensuring the USV's safety. We further validated our pipeline's effectiveness in underway replenishment and canal scenarios, simulating relevant marine tasks.

^{*}Indicates equal contribution. Authors are listed alphabetically.

[†]Corresponding author

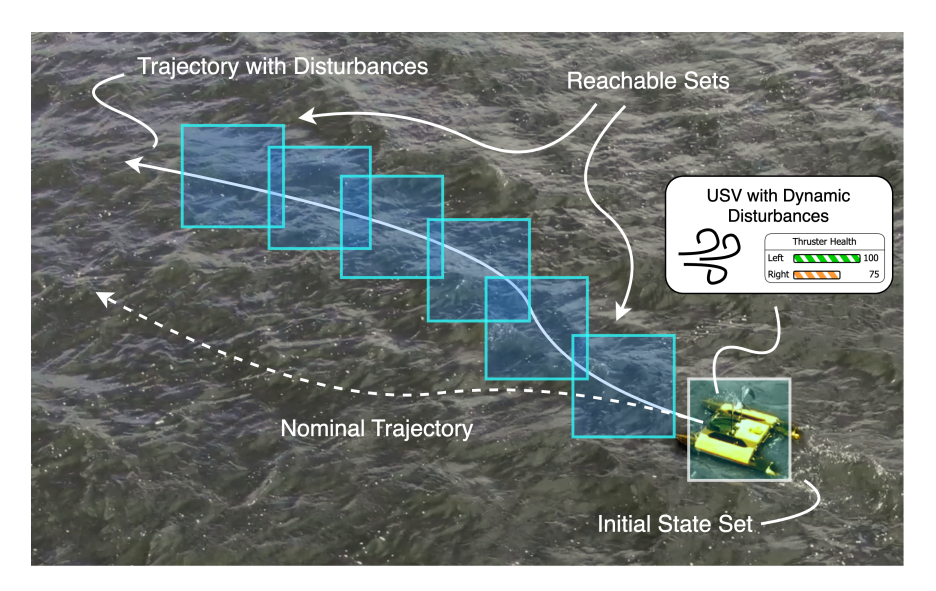


Figure 1: A diagram showing our approach to control and safety certification applied to a Clearpath Heron USV. The goal of the controller is to overcome disturbances and keep the trajectory with disturbances close to the nominal trajectory. The goal of reachability analysis is to generate reachable sets that bound the true (i.e., disturbed) trajectory.

1 Introduction

Marine robotics are an essential component of how we observe remote ocean phenomena and defend national interests (Yuh et al., 2011; Zereik et al., 2018; Pedrozo, 2023). Due to the large spatiotemporal scale of ocean activity, there is a need for marine robots that can be deployed for long periods of time and cover increasingly large areas (Rynne and von Ellenrieder, 2009). In addition, these vehicles are periodically expected to precisely navigate waterways or maneuver in close proximity to another vehicle if, for example, refueling in the field is necessary. The difficulty of these types of high-risk operations presents a barrier to fielding fully autonomous uncrewed surface vehicles (USVs). In the case of crewed vessels, the ship is usually carefully driven by a human operator when passing through a canal or close to another vessel, even though an autopilot capability is typically used in the open water. Furthermore, USVs that operate in marine environments, such as USVs, are often exposed to stochastic motion from wind, waves, and currents, and may be subject to actuator degradation due to biofouling or mechanical deterioration (Haldeman et al., 2016). The unknown nature of these disturbances creates challenges not only in how to effectively control a vehicle, but also in how to certify that the autonomous system satisfies safety constraints associated with the system and its environment. The control and safety certification challenges must be addressed to ensure autonomous marine vehicles can successfully complete tasks that require precise tracking, possibly during long missions during which a wide range of possible disturbances may influence the vehicle over time. Therefore, as we deploy autonomous vehicles on increasingly complex and long-range missions, it is critical to develop autonomy pipelines that consider the disturbances acting on the system to provide effective control and safety certification throughout all portions of a mission.

Many approaches have been developed to control USVs, including various forms of robust (Fossen, 1994) and adaptive (Yoerger and Slotine, 1991) control policies. The uncertainty of the disturbances and the nonlinear nature of USV dynamics make robust control difficult, especially when actuator dynamics are considered (Yoerger and Slotine, 1991; Fossen and Fjellstad, 1993; Whitcomb and Yoerger, 1996; McFarland and Whitcomb, 2014). In contrast, adaptive control can be used to quickly react to dynamic disturbances and model uncertainty by including additional terms parameterized by weights on generic function approximators such as Gaussian basis functions (Shen et al., 2020) or neural networks (Woo et al., 2018). While adaptive control has been well studied in theory (Fossen and Fjellstad, 1995; Lavretsky and Wise, 2012), its application to USVs has been limited to only a small number of studies with vehicles in test tanks or pools (Yoerger and Slotine, 1991), or to short field demonstrations that are limited in scope (Liu et al., 2021) and (Fischer et al., 2014). In this work, we add to the literature on adaptive control for USVs by reporting field results from new and more complex missions that are more relevant to fielded applications.

In addition to developing a controller, it is also important to ensure that the USV remains safe in various scenarios. During its mission, a USV may be tasked with navigating around obstacles (Polvara et al., 2018) or performing complex maneuvers such as underway replenishment (UNREP) (Miller et al., 1987). These situations are unavoidable since vessels often depart from harbors or pass through canals where they must navigate at least some of the way under their own power; the consequences of failure are enormous (Lee and Wong, 2021; Frittelli et al., 2024). The task of UNREP is particularly difficult since it requires precise coordination between vehicles, yet may be executed on missions that require sustained long deployments away from safe harbors. In such scenarios, it is critical to the safety of the system that collisions with other objects in the water are avoided, thus necessitating some method of certifying that the USV is safe in the sense that there is a low probability that the vehicle moves outside of the prescribed safe region within a given time horizon.

Given the uncertainty from the unknown nature of disturbances on the USV, as well as uncertainty due to imperfect state estimation, this is a challenging problem. To this end, we formulate the general problem of safety as a *reachability analysis* problem, and do so in a new way that is computationally tractable while capturing the uncertainty and complexity required for field deployments of USVs.

Reachability analysis (Bansal et al., 2017; Everett et al., 2021a; Sidrane et al., 2022) provides safety certification given a known model and an imperfect state estimate by constructing *reachable sets* that bound the possible future states of the system over some time horizon, as shown in Figure 1. By checking that the reachable sets do not overlap with an unsafe region of the state space, such as an area occupied by a ship or obstacle, reachability analysis can be used to certify safety. While existing reachability approaches are capable of handling disturbances, they assume knowledge of a set of possible disturbances. To account for all possible disturbances that could affect a system carrying out a long-range mission, this disturbance set would be very large, leading to overly conservative reachable sets that assume worst-case conditions at all times. Thus, we develop a reachability analysis approach that uses real-time information to provide reasonable estimates of the reachable sets for safety certification of a USV given the current understanding of disturbances acting on the system.

This work considers the challenges posed by control design and safety certification for USVs. To address the challenge of controlling USVs in the presence of disturbances, this paper describes a model reference adaptive control (MRAC) formulation similar to (Lavretsky and Wise, 2012) wherein an adaptive term in the inner loop controller helps the system achieve the desired tracking response. To address the problem of safety verification in the presence of disturbances, we use a formulation introduced in (Rober et al., 2024) where a moving horizon estimator (MHE) estimates the disturbances acting on the USV, which can be incorporated into a real-time reachability calculation to predict the future motion of the vehicle. This paper extends (Rober et al., 2024) by detailing the adaptive control law and show-casing extensive hardware experiments with a wide variety of disturbances that demonstrate how both the controller and reachabilty module are capable of adapting to changing disturbances that significantly affect the USV's dynamics. The presented methods are applicable to USVs in general, but are particularly helpful for USVs subject to widely varying disturbances or model uncertainty, such as those tasked for long-range missions where precise tracking and safety assurances are sometimes required. With this in mind, we also demonstrate our algorithms in two scenarios relevant to long-range missions, including canal passage and UNREP. The main contributions of our work can be summarized as follows:

- We demonstrate the application of an MRAC formulation, specifically MRAC augmentation of optimal baseline controller, to a USV operating in an environment with dynamic and unknown disturbances. Our controller shows improvement over a well-established PID control formulation, demonstrating better performance in the presence of real-world disturbances such as thruster faults, wind, currents, and drag forces.
- We develop a new reachability module that employs forward reachability analysis with real-time disturbance
 estimation to provide up-to-date certificates of the system's safety with respect to specified constraints. Our
 method can display to a supervisor the effect of insurmountable disturbances on the USV's performance.

We leverage a user-designed reference model in both our MRAC and real-time reachability approach. In the MRAC formulation, the objective of the adaptive controller is to drive the error between the reference model and the actual

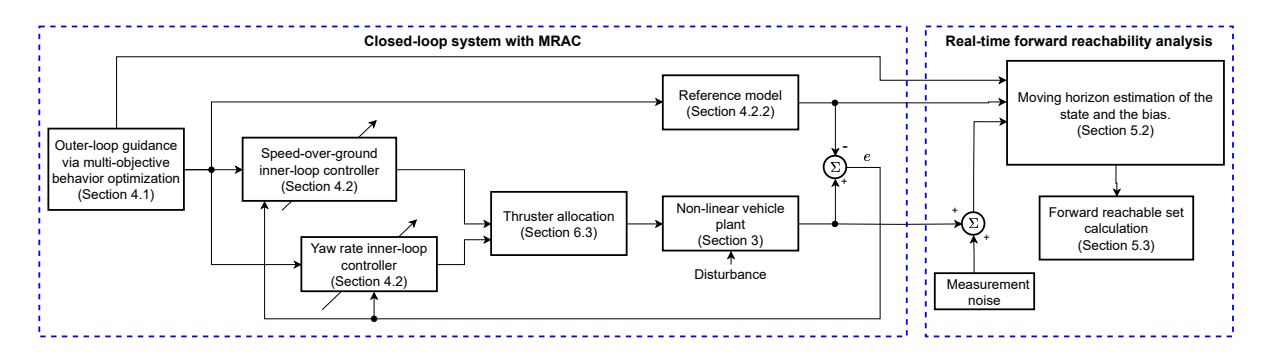


Figure 2: The block diagram of the control and reachability analysis architecture. The reference model is used in both the MRAC approach and the forward reachability analysis with the MHE.

vehicle plant asymptotically to zero. At the same time, the MHE estimates the bias between the reference model and the plant using recently observed data. The estimated bias and bias uncertainty are then used in the forward reachability analysis. Thus, the forward reachable sets are conservative in part because it is assumed that the bias could grow over the reachable set horizon, when in fact as time progresses the controller will be adapting with the goal to drive the reference model bias asymptotically to zero. An overview of this system architecture is shown in Figure 2, and more detailed block diagrams are included in Appendix A and Appendix B.

2 Related Work

2.1 Adaptive Control in Marine Vehicles.

The theoretical foundations of modern adaptive control were formed in the late 1970s and 1980s, and during this period researchers integrated similar but disconnected techniques for specific systems into a more unified framework for mathematical analysis of adaptive systems (Narendra et al., 1985; Narendra and Annaswamy, 2005). The first experiments using adaptive control for marine robotics followed thereafter in the 1990s and 2000s (Yoerger and Slotine, 1991), (Antonelli et al., 2001), (Skjetne et al., 2004), (Smallwood and Whitcomb, 2004). These first experiments were confined to test tanks, and in the case of underwater vehicles, performance was limited by the lack of sensors to directly measure the vehicle-relative translational velocity in the horizontal plane (Fossen and Fjellstad, 1995). However, these pioneering studies demonstrated the superior performance of adaptive control when compared with PD control in situations where precise navigation is required for a system with unknown nonlinear dynamics.

Adaptive control is well suited for the task of precise navigation in marine robotics, and previous work falls into two main categories: indirect and direct adaptive control (Narendra and Annaswamy, 2005). In the case of indirect adaptive control, estimation of the entire plant model is done simultaneously (or offline) with feedforward control (McFarland and Whitcomb, 2014; Smallwood and Whitcomb, 2004). Learning the entire model of a marine vehicle online in real time can be challenging due to the presence of non-Gaussian sensor noise, unmodeled dynamics, and limited excitation (McFarland and Whitcomb, 2014; Harris et al., 2023). This difficulty can be mitigated in part by only estimating modeling error relative to a nominal (known) non-linear plant (Shen et al., 2020) or linearized plant (Liu et al., 2021). In contrast, direct adaptive control approaches do not explicitly identify the plant parameters. Instead, the controller is adjusted such that the closed-loop marine vehicle system tracks a desired signal (e.g., MRAC (Makavita et al., 2020)) or sliding surface (Yoerger and Slotine, 1991; Shen et al., 2020). Other types of direct adaptive controllers for marine vehicles include \mathcal{L}_1 control (Rober et al., 2022) and adaptive robust integral of the sign of the error (RISE) (Fischer et al., 2014). In this work we use a direct approach to adaptive control since it is difficult to accurately model the all different types of disturbances encountered in the field. More specifically, we implement an MRAC formulation where a baseline optimal linear quadratic regulator (LQR) controller is augmented by an adaptive term to compensate for a range of disturbances with unknown structure.

Despite the previous theoretical development and laboratory testing with marine vehicles, as well as similar develop-

ment for robotic arms (Slotine and Li, 1987), mobile ground robots (Fukao et al., 2000), and aerial vehicle applications (Dydek et al., 2013; Bolender et al., 2015), there are relatively few reports that describe the performance of adaptive controllers in the open water on deployed marine systems. Of the previously mentioned studies, only (Liu et al., 2021) and (Fischer et al., 2014) report results from limited field experiments. Although simulation studies are useful in validating the theoretical robustness and stability of adaptive controllers, successful transitions of these controllers onto real marine systems remain difficult. As a related point, adaptive control has not been widely adopted for commercial marine vehicles. More effort is required to address the gap between academic research and industry practice.

The work described herein begins to address this gap by describing the development and testing of direct adaptive control for a USV deployed in the Charles River. Although the Charles River does not meet the technical definition of open water, the portion of the river near the MIT sailing pavilion was an ideal location to perform the necessary iterations of the design-field-evaluate cycle in an outdoor environment for a small USV.

2.2 Forward Reachability Analysis and Safety Assurances

Safety assurances can generally be obtained using either testing/data collection (Koopman and Wagner, 2016; Huang et al., 2016), or formal analysis (Zhang et al., 2008; Weng et al., 2018; Xu et al., 2020; Tjeng et al., 2017; Katz et al., 2019). Testing-based approaches rely on collecting large amounts of data through simulation or deployment of a given system and evaluating if/how the system may fail. Testing-based approaches are incapable of providing guarantees about safety because it is generally impossible to cover all possible failure cases. Alternatively, formal methods can provide guarantees about a given system, but their practical application can be limited due to computational constraints or assumptions about the system that may not reflect its actual behavior. In this paper, we incorporate online data collection into a formal reachability analysis framework to verify the safety of a system, thus striking a balance between data-driven and formal methods.

In this work we define a USV operation to be safe if the USV does not collide with the shore or other vehicles during the mission. In the context of formal analysis, this problem is represented mathematically with a model of the dynamics of the vehicle, the action by the controller, and the environment. To certify safety we must determine if the state of the system, which evolves per the mathematical model of the vehicle dynamics and the control action, can enter a region in the environment that is deemed unsafe. The formal method for computing bounds for all possible future states of the vehicle, i.e. forward reachable sets, is reachability analysis. (Mitchell, 2007)

Reachability analysis, including Hamilton-Jacobi methods (Bansal et al., 2017; Evans, 1998), Lagrangian methods (Gleason et al., 2017), and more recent approaches developed for systems with neural networks (NNs) (Vincent and Schwager, 2021; Dutta et al., 2019; Huang et al., 2019; Ivanov et al., 2019; Fan et al., 2020; Xiang et al., 2020; Hu et al., 2020; Sidrane et al., 2022; Everett et al., 2021b), determines a set of possible future states, i.e., reachable sets), of a system given a set of possible initial states. While all reachability analysis techniques handle uncertainty in the state (reflected in the initial state set) and many consider process/measurement noise (Everett et al., 2021b; Bansal et al., 2017), they typically assume knowledge of the system's behavior under bounded uncertainty. Moreover, with a few exceptions (Lew and Pavone, 2021; Althoff and Dolan, 2014; Herbert et al., 2017), reachability analysis is often too computationally expensive for online implementation, especially when the system is high-dimensional.

In this work, we perform online reachability analysis of a system subject to disturbances that are unknown *a priori*. Reachable sets are calculated in real time by leveraging <code>jax_verify</code> (Deepmind, 2020), a computational graph analysis tool capable of efficiently providing output bounds of nonlinear functions. Disturbances acting on the system are estimated online via MHE (Allgöwer et al., 1999), and are incorporated into the reachability analysis to predict the behavior of the actual system.

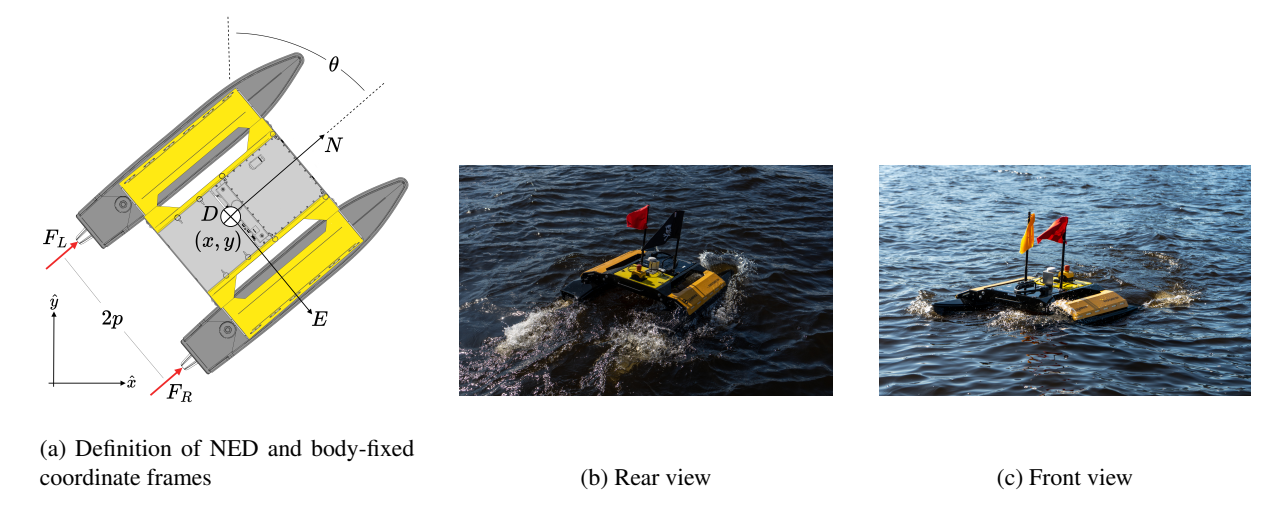


Figure 3: Clearpath Robotics Heron USV operated on the Charles River.

3 Model of USV Dynamics and Kinematics

The state of the USV is represented by

- $\eta = \begin{bmatrix} x & y & \theta \end{bmatrix}^T \in \mathbb{R}^2 \times \mathbb{S}^1$ where x and y denote the position of the USV in the north east down (NED) world frame, and θ is the USV's heading relative to true north as shown in Figure 3a
- $\nu = \begin{bmatrix} u & v & r \end{bmatrix}^T \in \mathbb{R}^3$ where u and v are the components of the translational velocity and r is the rotational velocity of the body expressed in the body-fixed frame.

For this class of catamaran USVs, the control inputs are the commanded rotational speed of the two thrusters. We define $\mathbf{u} = \begin{bmatrix} u_L & u_R \end{bmatrix}^T$ where u_L and u_R are the commanded thruster speeds respectively.

The standard model of kinematics and dynamics of USV motion are (Fossen, 1994)

$$\dot{\boldsymbol{\eta}} = \begin{bmatrix} \boldsymbol{R}(\boldsymbol{\theta}) & 0_{2\times 1} \\ 0_{1\times 2} & 1 \end{bmatrix} \boldsymbol{\nu},\tag{1}$$

$$\tau(\nu, u) = M\dot{\nu} + C(M, \nu)\nu + D(\nu)\nu - \tau_{dist}(\nu), \tag{2}$$

where $M \in \mathbb{R}^{3\times3}$ is the inertia matrix with rigid-body and added mass terms, $C(M, \nu) : \mathbb{R}^{3\times3} \times \mathbb{R}^{33} \to \mathbb{R}^{3\times3}$ is the Coriolis matrix, $D(\nu) \in \mathbb{R}^{3\times3}$ is the nonlinear drag matrix, and $\tau(\nu, u) = \begin{bmatrix} F_L + F_R & 0 & p(F_L - F_R) \end{bmatrix}^T \in \mathbb{R}^3$ is the control induced forces and moments acting on the body. All other unknown disturbances are captured by $\tau_{dist}(\nu)$. The rotation matrix $R(\theta) \in SO(2)$ is the kinematic relationship defined in Section 2.2.1 of (Fossen, 1994).

Herein the model (2) is expressed in two ways: 1) a pair of linearized systems about a trim condition is used to develop the adaptive controller, and 2) a discrete model of the closed loop system that includes the controller with uncertainty in observations is used to develop the reachability analysis. Both models retain a term related to the disturbance of the system.

3.1 Linearized Models

We define two linearized models of the dynamics of the Heron USV (2). There are decoupled models for both the speed dynamics and sway and yaw-rate dynamics. This separation is motivated by two factors: First, the Heron USV is underactuated since there are only two actuators, but the model (2) captures three degrees of freedom. Second,

the higher-level guidance algorithm, detailed in Section 4, only generates two reference signals: desired speed and trackline heading.

3.1.1 Linearized Speed Model

The speed over ground $u_{sog} = \sqrt{u^2 + v^2}$. We linearize the model (2) about a given non-zero trim condition of u_{sog} to find

$$\dot{u}_{sog} = a_{p_1} u_{sog} + b_{p_1} \Lambda_1 \left(u_{thr} + g_1 \left(u_{sog} \right) \right), \tag{3}$$

where $a_{p_1}, b_{p_1} \in \mathbb{R}$ are nominal model parameters identified a priori, $\Lambda_{p_1} \in \mathbb{R}_+$ is the unknown thrust control effectiveness modeling uncertainty, and $g_1(u_{sog}) : \mathbb{R} \to \mathbb{R}$ is the unknown parametric matched uncertainty.

The control input $u_{thr} \in \mathbb{R}$ is applied equally to each thruster.

3.1.2 Linearized Sway Yaw-Rate Model

The sway and yaw-rate model (2) are linearized about the trim condition of v = 0 and r = 0. The resulting linearized model is

$$\begin{bmatrix} \dot{v} \\ \dot{r} \end{bmatrix} = A_p \begin{bmatrix} v \\ r \end{bmatrix} + B_p \Lambda_{p_2} (u_{rud} + g_2(r)), \tag{4}$$

where $A_p \in \mathbb{R}^{2 \times 2}$ is an constant state transition matrix identified a priori, $B_p \in \mathbb{R}^{2 \times 1}$ is the constant and known control effectiveness matrix, $\Lambda_{p_2} \in \mathbb{R}_+$ is the unknown thrust control effectiveness modeling uncertainty, and $g_2(r)$: $\mathbb{R} \to \mathbb{R}$ is the unknown parametric matched uncertainty.

3.1.3 Discussion

The transformation of the nonlinear model (2) into the two decoupled models of speed (3) and sway-heading (4) allows the control problem to be expressed in a 2D workspace (speed error and heading error). This approach is considered common practice in the literature (Fossen, 1994), but it has limitations. For instance, the disturbances that act in the sway degree of freedom are not captured in either $g_1(u_{sog})$ nor $g_2(r)$. This limitation has no practical consequence since the Heron USV is not directly actuated in the sway degree of freedom. Another limitation of this approach is that more complex disturbances, such as those that are nonlinear functions of both u_{sog} and r, are not captured; we leave this issue for future work. Finally, the formulation assumes the disturbances in the plant model (2) can be represented in the linearized models by terms $g_1(u_{sog})$ or $g_2(r)$ which act in the control space of u_{thr} and u_{rud} respectively.

3.2 Discrete Closed-Loop Model

Consider a state-feedback controller $u_t = \pi(x_t)$, which is described later in Section 4. The closed loop dynamics of the system (1) and (2) with the control policy $\pi(x_t)$ can be expressed as a discrete general nonlinear function with a disturbance term $\mathbf{w} \in \mathbb{R}^6$.

$$\boldsymbol{x}_{t+1} = \begin{bmatrix} \boldsymbol{\eta}_{t+1} \\ \boldsymbol{\nu}_{t+1} \end{bmatrix} = f_{cl}(\boldsymbol{x}_t; \boldsymbol{\pi}) + \boldsymbol{w}_t$$
 (5)

$$\boldsymbol{y}_t = h(\boldsymbol{x}_t) + \boldsymbol{w}_{y_t}, \tag{6}$$

where $y_t \in \mathbb{R}^{n_y}$ is the measured system corrupted by noise w_{y_t} .

In this work we assume $\mathbf{w}_t \sim \mathcal{N}(\boldsymbol{\mu}_t, \boldsymbol{W}_t)$ and $\mathbf{w}_{y_t} \sim \mathcal{N}(\mathbf{0}, \boldsymbol{W}_{y_t})$. Furthermore, we assume that \boldsymbol{W}_t is diagonal. Since the additive bias to the nominal system dynamics \mathbf{w}_t is time-varying, we impose a condition that

$$|(\boldsymbol{\mu}_{t+1})_i - (\boldsymbol{\mu}_t)_i| \le \Delta \boldsymbol{\mu}_i |(\boldsymbol{\sigma}_{t+1})_i - (\boldsymbol{\sigma}_t)_i| \le \Delta \boldsymbol{\sigma}_i,$$

$$(7)$$

where $(\sigma_t)_i \in \mathbb{R}$ for $i = 1, ..., n_x$ is the standard deviation associated with the covariance matrix W_t , i.e., $(W_t)_{ii} = (\sigma_t)_i^2$, and $\Delta \mu_i, \Delta \sigma_i \in \mathbb{R}^{n_x}$ represent the bounded possible variation in μ_t and σ_t , respectively, per time step.

4 Control Architecture

The design of the control system can be divided into two levels:

- Outer-loop guidance algorithms as behaviors that generate a reference trajectory from mission objectives.
- Inner-loop controllers that are designed to drive the actual state of the vehicle to the reference trajectory.

Guidance algorithms are more specific to the mission requirements and we report three different algorithms used in the experiments. The implementation of LQR-proportional-integral (PI) and MRAC inner-loop controllers are subsequently described.

4.1 Guidance Behavior Design

In this work the guidance algorithms were implemented as behaviors within the Interval Programming (IvP) multiobjective behavior optimization architecture MOOS-IvP (Benjamin et al., 2010). The optimization is stated as

$$u_{DES}, \theta_{DES} = \underset{u \in S_u, \ \theta \in S_\theta}{\operatorname{arg max}} \sum_{q=1}^{N_{active}} w_q f_q(\eta, \nu)$$
(8)

where u_{DES} is the desired speed selected from domain S_u , θ_{DES} is the desired heading selected from domain S_θ . The optimization is over the sum of N_{active} utility functions $f_q(\eta, \nu)$ each generated by a behavior and also weighted by w_q . Details regarding the specific behaviors used in this work are described in Section 4.1.

The following sections outline the guidance algorithms used in the experiments described in Sections 8 and 9. The baseline track-line following behavior is a PD controller that enables straight line tracking. L_1 Guidance (Park et al., 2004) was used for more complex smooth paths. The method in (Skejic et al., 2009) enabled the Underway Replenishment missions.

4.1.1 Baseline Track-line Following

The objective of the baseline track-line guidance algorithm is to have the vehicle track a user-selected path in the Earth-fixed frame using a proportional derivative (PD) error feedback approach. The baseline track-line following guidance algorithm is described in (Benjamin, 2024, Section 9.7).

4.1.2 L1 Guidance

The L_1 guidance algorithm (Park et al., 2004) has the same objective as the baseline track-line following algorithm described in Section (4.1.1), but is better suited for missions with more complex (e.g., curved) paths (Park et al., 2004). The approach was modified to realize the improvement on track-line following for the underactuated Heron USV. Specifically, in (Park et al., 2004) the term related to lateral (i.e., sway) acceleration command is

$$a_{cmd} = 2\frac{u_{sog}^2}{L_1}\sin\eta,\tag{9}$$

where $L_1 \in \mathbb{R}_{\geq 0}$ is the length of a line from ownship position to a reference point on the desired trajectory and η is the angle between the course over ground and the line. However, the Heron USV is not actuated in the sway direction

and cannot generate a lateral acceleration directly. The vehicle, however, may rotate while moving at speed u_{sog} to generate lateral acceleration. Using the coupling of angular and forward velocities, the desired yaw rate command is

$$r_{cmd} = 2\frac{u_{sog}}{L_1}\sin\eta. ag{10}$$

While this guidance algorithm is similar to approaches such as proportional guidance and line-of-sight guidance for certain paths, it includes a lookahead element that enables tight tracking on curved trajectories.

4.1.3 Underway Replenishment (UNREP)

As described in Section 9.1, the UNREP mission requires a follower vessel to maneuver alongside a lead vehicle and maintain a constant relative position and heading to transfer goods between two vessels. The objective of the target tracking for UNREP guidance is to minimize errors in both the cross-track and inline degrees of freedom. In this study we use the algorithm presented in (Skejic et al., 2009) to perform the UNREP mission.

4.1.4 Heading to Yaw Rate Controller

The optimizer in the IvPHelm (Benjamin et al., 2010) combines the output from individual behaviors into a single decision of heading and speed. Optimization is performed over discrete domain intervals, and by definition the raw output from IvPHelm is discontinuous. To address this issue, the discrete output from the IvPHelm is filtered to generate a smooth reference trajectory for the inner-loop controller. Given a decision from the IvPHelm of u_{DES} and θ_{DES} , the reference trajectories for speed u_{des} and yaw rate r_{des} are defined as

$$\begin{bmatrix} \dot{q}_1 \\ \dot{q}_2 \end{bmatrix} = \begin{bmatrix} -\frac{1}{\tau_u} & 0 \\ 0 & -\frac{1}{\tau_r} \end{bmatrix} \begin{bmatrix} q_1 \\ q_2 \end{bmatrix} + \begin{bmatrix} u_{DES} \\ \tau_{\theta} \Delta \theta \end{bmatrix}$$
(11)

$$\begin{bmatrix} u_{des} \\ r_{des} \end{bmatrix} = \begin{bmatrix} \frac{1}{\tau_u} & 0 \\ 0 & \frac{1}{\tau_r} \end{bmatrix} \begin{bmatrix} q_1 \\ q_2 \end{bmatrix}$$
 (12)

where $\Delta\theta$ is computed using the following method: Let

$$m{e}_{ heta} = egin{bmatrix} \sin\left(heta
ight) \\ \cos\left(heta
ight) \\ 0 \end{bmatrix}, \quad ext{and} \quad m{e}_{ heta_{DES}} = egin{bmatrix} \sin\left(heta_{DES}
ight) \\ \cos\left(heta_{DES}
ight) \\ 0 \end{bmatrix},$$

and $e_{err} = e_{\theta} \times e_{\theta_{DES}}$ be the unit vectors in the direction of the current vehicle heading, desired heading, and cross product of the two vectors respectively. Then

$$\Delta \theta = \arccos(e_{\theta}^T e_{\theta_{DES}}) \cdot (-\operatorname{sgn}(e_{err_3}))$$
(13)

4.2 Control Design

The following section describes the structure of the inner-loop controllers used to facilitate the tracking of the reference trajectory from the guidance behaviors. The synthesis of the speed controller and sway and yaw-rate controller is identical. For brevity, this section only presents the development of the more complex sway and yaw-rate controller. Implementation details are provided for both controllers in Section 6.

We present the formulation for the yaw-rate controller, which is identical to the speed controller development.

Consider the linearized model of USV motion in the sway and yaw-rate degrees of freedom (4) where the uncertainty is parameterized as

$$g_2(r) = \mathbf{\Theta}^T \mathbf{\Phi}(r) \tag{14}$$

where $\Theta \in \mathbb{R}^N$ is a vector of unknown constant parameters, and $\Phi(r) : \mathbb{R} \to \mathbb{R}^N$ is the known and locally Lipschitz N-dimensional regression vector. The linearized dynamics (4) are expressed as

$$\begin{bmatrix} \dot{v} \\ \dot{r} \end{bmatrix} = A_p \begin{bmatrix} v \\ r \end{bmatrix} + B_p \Lambda_{p_2} \left(u_{rud} + \mathbf{\Theta}^T \mathbf{\Phi} \left(r \right) \right)$$
(15)

In the case of the linearized model of the Heron USV (4) the pair $(A_p, B_p \Lambda_{p_2})$ is controllable. (See Section 6.2 for details.)

The desired control objective is to perform command tracking, meaning the control input u must be enable $y \in \mathbb{R}$ defined as

$$y \triangleq C_p \begin{bmatrix} v \\ r \end{bmatrix}, \tag{16}$$

to track the bounded and time-varying command $y_{cmd_r} = r_{des} \in \mathbb{R}$ as defined in Section 4.1.4, with bounded errors in the presence of system uncertainties in $\{A_p, \Lambda, \Theta\}$. Furthermore, $C_p = \begin{bmatrix} 0 & 1 \end{bmatrix}$ is known and constant). The integrated error that facilitates output tracking is

$$e_{yI} = \int_0^t \left(y(\tau) - y_{cmd_r}(\tau) \right) d\tau. \tag{17}$$

To facilitate the tracking objective, the dynamics are expressed in the extended open-loop form (Lavretsky and Wise, 2012, Chapter 10) as

$$\begin{bmatrix} \dot{e}_{yI} \\ \dot{v} \\ \dot{r} \end{bmatrix} = \underbrace{\begin{bmatrix} 0 & C_p \\ 0_{2\times 1} & A_p \end{bmatrix}}_{A} \begin{bmatrix} e_{yI} \\ v \\ r \end{bmatrix} + \underbrace{\begin{bmatrix} 0 \\ B_p \end{bmatrix}}_{B} \Lambda_{p_2} \left(u + \mathbf{\Theta}^T \mathbf{\Phi} \left(r \right) \right) + \underbrace{\begin{bmatrix} -1 \\ 0_{2\times 1} \end{bmatrix}}_{B_{ref}} y_{cmd}, \tag{18}$$

The controller u_{rud} for the yaw-rate dynamics is the sum of the baseline controller u_{bl} and an adaptive component u_{ad} which are subsequently defined:

$$u_{rud} = u_{bl} + u_{ad}. (19)$$

4.2.1 Baseline Optimal LQR PI Controller

First, the baseline controller u_{bl} is constructed. Consider the dynamics in (18) where $\Lambda_{p2} = 1$ and $\Theta = 0_{N \times 1}$ as

$$\begin{bmatrix} \dot{e}_{yI} \\ \dot{v} \\ \dot{r} \end{bmatrix} = A \begin{bmatrix} e_{yI} \\ v \\ r \end{bmatrix} + Bu + B_{ref} y_{cmd}, \tag{20}$$

Using the extended form of the dynamics in (20), a LQR PI feedback controller was designed using the robust LQR PI servomechanism design (Lavretsky and Wise, 2012, Eqs. 10.37-10.43). The baseline component of the controller $u_{bl} \in \mathbb{R}$ is

$$u_{bl} \triangleq -\boldsymbol{K}_{LQR}^{T} \begin{bmatrix} e_{yI} \\ v \\ r \end{bmatrix} . \tag{21}$$

The baseline controller enables the system to perform reference command tracking without model uncertainty (e.g. control effectiveness and matched uncertainty). The aforementioned modeling errors are expected to degrade controller performance.

4.2.2 Adaptive Augmentation of Optimal Baseline Controller

The baseline controller u_{bl} is designed to provide desired system responses (e.g., rise time, overshoot, and bandwidth). However, adding uncertainty degrades the desired response. Hence, the subsequent adaptive controller design will facilitate restoration of the degraded system response.

Consider the reference model dynamics

$$\begin{bmatrix} \dot{e}_{yI_{ref}} \\ \dot{v}_{ref} \\ \dot{r}_{ref} \end{bmatrix} = A_{ref} \begin{bmatrix} e_{yI_{ref}} \\ v_{ref} \\ r_{ref} \end{bmatrix} + B_{ref} y_{cmd_r}, \tag{22}$$

where $A_{ref} \triangleq A - BK_{LQR}^T$. The reference model dynamics represent the system response using only the baseline controller, i.e. $u = u_{bl}$, and without modeling errors. i.e. $\Lambda = 1$ and $\Theta = 0_{N \times 1}$.

In the presence of model uncertainty, an adaptive control term u_{ad} to augment the baseline controller is constructed. The adaptive augmentation component is designed as

$$u_{ad} = -\hat{\overline{\Theta}}^T \overline{\Phi} (u_{bl}, r), \qquad (23)$$

where $\widehat{\Phi} \in \mathbb{R}^{N+1}$ is an adaptive term that compensates for an extended matrix of unknown parameters, and $\overline{\Phi}(u_{bl}, r) : \mathbb{R} \times \mathbb{R}^N \to \mathbb{R}^{N+1}$ is a regression matrix defined as

$$\overline{\mathbf{\Phi}}\left(u_{bl},\,r\right) \triangleq \left[u_{bl},\,\mathbf{\Phi}\left(r\right)^{T}\right]^{T}.\tag{24}$$

Following the development in (Lavretsky and Wise, 2012, Ch. 10.3), the continuous-time adaptive update law is designed as

$$\dot{\widehat{\mathbf{\Theta}}} = -\Gamma_{\Theta} \overline{\mathbf{\Phi}} \left(u_{bl}, \, r \right) \mathbf{e}^T P B,\tag{25}$$

where $e \triangleq \begin{bmatrix} e_{yI} \\ v \\ r \end{bmatrix} - \begin{bmatrix} e_{yI_{ref}} \\ v_{ref} \\ r_{ref} \end{bmatrix}$, the adaptation gain $\Gamma_{\Theta} \in \mathbb{R}^{(N+1)\times(N+1)}$, and $P \in \mathbb{R}^{3\times3}$ is a positive definite solution to the Lyapunov equation

$$PA_{ref} + A_{ref}^T P = -Q, (26)$$

for a user-selected positive definite $Q \in \mathbb{R}^{3\times 3}$.

4.2.3 MRAC Implementation for Heron USV

The controller that is applied to the system is the sum of the baseline and adaptive controller

$$u = u_{bl} + u_{ad}. (27)$$

The stability analysis for this controller and dynamics can be found in (Lavretsky and Wise, 2012, Ch. 10). This base-line adaptive controller with adaptive augmentation architecture was used for both speed and yaw rate tracking control objectives. In Section 6 we report the numerical values used for controller implementation. The baseline controller, adaptive controller, and adaptive updates laws were designed in continuous-time; however, they were implemented in discrete-time using forward Euler integration.

5 Real-Time Forward Reachability Calculation

In this section describes the formulation introduced in (Rober et al., 2024) for discrete-time forward reachability analysis to determine the safety of our system in the face of *a priori* unknown disturbances, which are estimated online. We later build on this work by demonstrating the effectiveness of this real-time reachability formulation on a diverse set of fielded experiments.

We define the forward reachable set at time t+1 of the system with initial state set \mathcal{X}_0 and closed loop dynamics model $f_{cl}(\boldsymbol{x}_t;\pi)$ in (6) as

$$\mathcal{R}_{t+1}(\mathcal{X}_0) = f_{cl}(\mathcal{R}_t(\mathcal{X}_0); \pi). \tag{28}$$

where $\mathcal{R}_0(\mathcal{X}_0) = \mathcal{X}_0$ and $f_{cl}(\mathcal{R}_t(\mathcal{X}_0); \pi)$ is shorthand for $\{f_{cl}(\mathbf{x}_t; \pi) \mid \mathbf{x}_t \in \mathcal{R}_t(\mathcal{X}_0)\}$. The exact reachable set \mathcal{R}_t is expensive to compute. Instead, we compute reachable set over-approximations (RSOAs), i.e., $\overline{\mathcal{R}}_t \supseteq \mathcal{R}_t$, as is specified in Section 5.1. The RSOAs $\{\overline{\mathcal{R}}_t, \overline{\mathcal{R}}_{t+1}, \dots, \overline{\mathcal{R}}_{t+\tau_r}\}$, denoted as $\overline{\mathcal{R}}_{t:t+\tau_r}$, are used to verify safety of the system over a horizon τ_r by checking if the future states can reach an unsafe region of the state space $\mathcal{C} \subset \mathbb{R}^3$. If there is an $i \in \mathcal{T} = \{t, \dots, t+\tau_r\}$ such that $\overline{\mathcal{R}}_i \cap \mathcal{C} \neq \emptyset$, the system may enter the unsafe region and safety is not guaranteed.

Note that while RSOAs are capable of verifying safety, more conservative RSOAs make the verification conditions more difficult to satisfy, so tight RSOAs are preferred.

Our approach is designed to be executed online, regularly generating RSOAs over a finite time horizon at a fixed interval. The proposed data-driven reachability approach is summarized as:

- 1. First, before the deployment of the system, a computational graph (CG) is constructed to represent the system dynamics f_{cl} .
- 2. At each time step during runtime, we use the MHE to obtain an estimate of the state \hat{x}_t and estimates of the most recent mean and covariance values of w_t .
- 3. Finally, the mean and covariance estimates from the MHE are input into a CG relaxation to conduct reachability analysis, thus predicting the behavior of the actual system.

5.1 Computational Graphs and Linear Relaxation

A computational graph (CG) G is a directed acyclic graph with nodes $V = \{V_1, V_2, ..., V_n\}$ and edges E. Each edge connects a pair of two nodes (V_i, V_j) where the output of V_i is the input to V_j . Each node is associated with a basic computation function $G_i(\cdot)$. We define the output of node V_i as

$$g_i^G = G_i(u(V_i)) \tag{29}$$

where $u(V_i)$ is the set of inputs to V_i or equivalently, the outputs from nodes with edges directed toward V_i . Let the inputs to the graph G be $\mathbf{z} \in \mathbb{R}^{n_i}$ and the graph has single output node V_o with $\dim(V_o) = \mathbb{R}^{n_o}$. Using this, the output of node V_i as a function of \mathbf{z} , i.e. $g_i^G = g_i^G(\mathbf{z})$. Hence, the output of the computational graph is g_o^G . Given a set of computational graph inputs \mathcal{I} , we want to describe the set of possible outputs $\mathcal{O} = \{g_o^G(\mathbf{z}_0) \mid \mathbf{z}_0 \in \mathcal{I}\}$. We construct \mathcal{I} as a hyper-rectangular set, defined by

$$\mathcal{B}_{\infty}(\overline{\mathbf{z}}_0, \epsilon) \triangleq \{ \mathbf{z} \mid \|(\mathbf{z} - \overline{\mathbf{z}}_0) \oslash \epsilon\|_{\infty} \le 1 \}, \tag{30}$$

where $\overline{\mathbf{z}}_0 \in \mathbb{R}^{n_i}$ is the center of the l_{∞} -ball, $\epsilon \in \mathbb{R}^{n_i}_{\geq 0}$ is a vector of radii for the corresponding elements of \mathbf{z} , and \oslash denotes element-wise division. Bound on the output set \mathcal{O} can be found using the following theorem.

Theorem 5.1 (Linear Relaxation of CGs, Thm. 2 (Xu et al., 2020)). Given a CG G and a hyper-rectangular set of possible inputs \mathcal{I} , there exist two explicit functions

$$g_{L,o}^{oldsymbol{G}}(oldsymbol{z}) = oldsymbol{\Psi} oldsymbol{z} + oldsymbol{lpha}, \quad g_{U,o}^{oldsymbol{G}}(oldsymbol{z}) = oldsymbol{\Phi} oldsymbol{z} + oldsymbol{eta}$$

such that the inequality $g_{L,o}^{G}(z) \leq g_{o}^{G}(z) \leq g_{U,o}^{G}(z)$ holds element-wise for all $z \in \mathcal{I}$, with $\Psi, \Phi \in \mathbb{R}^{n_o \times n_i}$ and $\alpha, \beta \in \mathbb{R}^{n_o}$.

These bounds on $g_o^G(z)$ allow us to define $\overline{\mathcal{O}}$, a hyper-rectangular over-approximation of the output set \mathcal{O} , as

$$\mathcal{O} \subseteq \overline{\mathcal{O}} = \{ \boldsymbol{o} \mid g_{L,o}^{\boldsymbol{G}}(\mathbf{z}) \le \boldsymbol{o} \le g_{U,o}^{\boldsymbol{G}}(\mathbf{z}), \ \exists \mathbf{z} \in \mathcal{I} \}.$$
(31)

To conduct reachability analysis, we generate RSOAs using the CG analysis tool <code>jax_verify</code> (Deepmind, 2020). Other CG analysis tools, such as Auto-LiRPA (Xu et al., 2020) could also be used, but <code>jax_verify</code> supports just-in-time compilation and is thus fast enough to enable online computation. By specifying the control policy π and the discrete representation of the open-loop dynamics (3) and (4) as functions in the <code>jax_verify</code> framework, we can generate a CG representation of the discrete closed-loop model (6). Moreover, we can use results from Theorem 5.1 for linear relaxation (Xu et al., 2020) to obtain bounds on \hat{x}_{t+1} from a set of possible \hat{x}_t and thus find the RSOA for the closed-loop discrete Heron USV system model (6).

5.2 Moving Horizon Bias Estimation

To characterize disturbances to the system, we employ a moving horizon estimator (MHE) (Allgöwer et al., 1999) to estimate the difference between nominal system dynamics and the actual system behavior. This allows us to represent both internal changes to the system (i.e. thruster imbalances or inefficiencies) and external disturbances (i.e. wind or strong currents) as an additive bias to the nominal system dynamics. After collecting data measurements $y_{t-\tau_e:t}$ in a receding horizon window from time $t-\tau_e$ to t, we perform the following optimization to find estimates of the state \hat{x} and uncertainty about the state dynamics \hat{w}

$$\min_{\hat{\mathbf{x}}_{t-\tau_e;t},\hat{\mathbf{w}}_{t-\tau_e;t}} J,\tag{32}$$

where

$$J = \|\hat{\boldsymbol{x}}_t - \overline{\boldsymbol{x}}_t\|_{\boldsymbol{Q}_{t|t-1}^{-1}}^2 + \sum_{k=t-\tau_e}^t \|\boldsymbol{y}_k - h(\hat{\boldsymbol{x}}_k)\|_{\boldsymbol{W}_y^{-1}}^2 + \|\hat{\boldsymbol{w}}_k\|_{\boldsymbol{W}_k^{-1}}^2.$$
(33)

In (33), \overline{x}_t is the state estimate prior, $Q_{t|t-1} \in \mathbb{R}^{3\times 3}$ is the state uncertainty prior, and $\|\hat{x}_t - \overline{x}_t\|_{Q_{t|t-1}^{-1}}^2 \triangleq (\hat{x}_t - \overline{x}_t)^\top Q_{t|t-1}^{-1}(\hat{x}_t - \overline{x}_t)$. The result of (32) are values of $\hat{x}_{t-\tau_e:t}$ and $\hat{w}_{t-\tau_e:t}$ that optimally estimate the state and disturbance terms over the given window. Much like model predictive control (Borrelli et al., 2017), the typical motivation for using a MHE is to execute (32) at each discrete time step to determine \hat{x} . Each iteration of the process calculates a new estimate of \hat{x} with (32), and the priors of the state estimate \overline{x}_{t+1} and covariance $Q_{t+1|t}$ are generated for the next time step using the update law

$$\overline{x}_{t+1} = f_{cl}(\hat{x}_t; \pi) + \hat{w}_t \tag{34}$$

$$Q_{t|t} = \left(Q_{t|t-1}^{-1} + H^{\top} R^{-1} H\right)^{-1}$$
(35)

$$Q_{t+1|t} = AQ_{t|t}A^{\top} + W_t, \tag{36}$$

where $\boldsymbol{A} = \frac{\partial f_{cl}}{\partial \boldsymbol{x}}\big|_{\boldsymbol{x} = \hat{\boldsymbol{x}}_t}$, $\boldsymbol{H} = \frac{\partial h}{\partial \boldsymbol{x}}\big|_{\boldsymbol{x} = \hat{\boldsymbol{x}}_t} = \boldsymbol{I}_{3 \times 3}$ and $\boldsymbol{R} \in \mathbb{R}^{3 \times 3}$ is the noise covariance matrix for measurement sensing error.

5.3 Reachable Set Calculation

At each time step t, the forward reachable sets are calculated using the CG assembled before the mission and the results from the MHE that are updated in real time. As described in Section 5.2, we collect the state estimate \hat{x}_t and generate the posterior \overline{x}_{t+1} per equation (34). We also make the approximations $\hat{\mu}_t = \text{mean}(\hat{w}_{t-\tau_e:t})$ and $\hat{W}_t = \text{cov}(\hat{w}_{t-\tau_e:t})$.

Computational Graph with Augmented State

Since in this formulation of forward reachabilty analysis we consider a (bounded) range of possible future disturbances given (7), we augment the state input to the CG by the addition of terms for the disturbance and its assumed rate of change. We also add into our augmented state the rate of change of the standard deviations associated with each state, which remain constant over the time horizon. Thus, we introduce the augmented CG G_{cl} with input

$$\overline{z}_{t} = \begin{bmatrix} \tilde{x}_{t} \\ \tilde{\mu}_{t} \\ \mathring{\mu}_{t} \\ \mathring{\sigma}_{t} \end{bmatrix} \quad \text{and output denoted} \quad g_{o}^{G_{cl}}(\overline{z}_{t}) = \begin{bmatrix} \tilde{x}_{t+1} \\ \tilde{\mu}_{t+1} \\ \mathring{\mu}_{t+1} \\ \mathring{\sigma}_{t+1} \end{bmatrix}, \tag{37}$$

where $\tilde{x}_t, \tilde{\mu}_t, \mathring{\mu}_t, \mathring{\sigma}_t \in \mathbb{R}^6$. Note that while the inputs $\tilde{x}_t = \hat{x}_t$ and $\tilde{\mu}_t = \hat{w}_t$ as computed via the MHE, the inputs $\mathring{\mu}_t$ and $\mathring{\sigma}_t$ are internal to the reachability analysis and are used to account for the time variation of μ_t and W_t as described by (7). G_{cl} is then manually constructed with the equations

$$\tilde{\boldsymbol{x}}_{t+1} = f_{cl}(\tilde{\boldsymbol{x}}_t; \pi) + \tilde{\boldsymbol{\mu}}_t \tag{38}$$

$$\tilde{\boldsymbol{\mu}}_{t+1} = \tilde{\boldsymbol{\mu}}_t + \mathring{\boldsymbol{\mu}}_t + \gamma \mathring{\boldsymbol{\sigma}}_t \tag{39}$$

$$\mathring{\boldsymbol{\mu}}_{t+1} = \mathring{\boldsymbol{\mu}}_t \tag{40}$$

$$\mathring{\boldsymbol{\sigma}}_{t+1} = \mathring{\boldsymbol{\sigma}}_t, \tag{41}$$

where $\gamma > 0$ is a parameter used to *concretize* an uncertainty bound for a selected confidence interval, e.g., $\gamma = 3$ means we assume all samples fall within three standard deviations of the mean. Concretization is done because jax_verify (and many other analysis tools, such as (Xu et al., 2020)) assumes concrete bounds on the possible input states.

5.3.2 Algorithm Outline

Having constructed G_{cl} and established how we use the MHE, we can now explicitly specify our approach, which is summarized pictorially in Figure 4 and via pseudo-code in Algorithm 1.

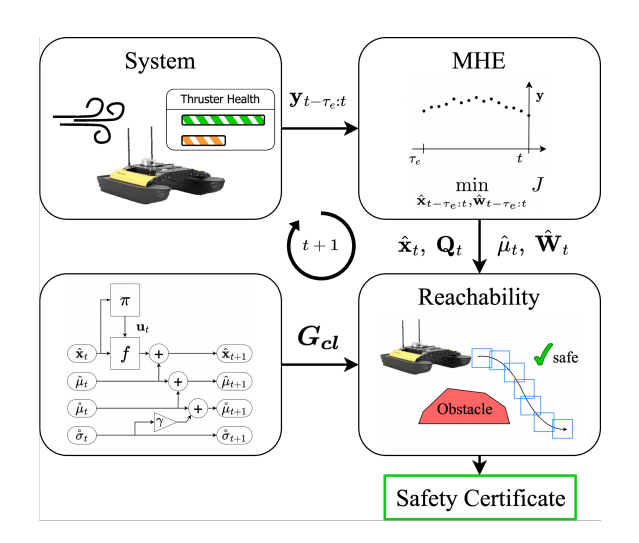


Figure 4: Block diagram depicting our approach (Rober et al., 2024). Data is collected from the system and fed into the MHE, which estimates the state and disturbance terms. The outputs of the MHE are used with a CG representation of the closed-loop dynamics to conduct reachability analysis and certify safety.

Algorithm 1 Online Safety Certification

Input: computational graph G_{cl} , reachability horizon τ_r , vehicle data $y_{t-\tau_e:t}$, concretization parameter γ , unsafe region \mathcal{C}

Output: safety certificate c over horizon τ_r

- 1: $c \leftarrow \text{true}$
- 2: $\hat{\boldsymbol{x}}_{t-\tau_e:t}, \hat{\boldsymbol{w}}_{t-\tau_e:t} \leftarrow \text{MHE}(\boldsymbol{y}_{t-\tau_e:t})$
- 3: $\boldsymbol{\mu}_t \leftarrow \mathtt{mean}(\hat{\boldsymbol{x}}_{t-\tau_e:t})$
- 4: $oldsymbol{W}_t \leftarrow ext{cov}(\hat{oldsymbol{w}}_{t- au_e:t})$
- 4: $\boldsymbol{W}_{t} \leftarrow \text{cov}(\boldsymbol{W}_{t-\tau_{e}:t})$ 5: $\boldsymbol{\epsilon}_{\boldsymbol{x}} \leftarrow \text{concretize}(\text{MHE}.\boldsymbol{Q}_{t}, \gamma)$ 6: $\boldsymbol{\epsilon}_{\boldsymbol{\mu}} \leftarrow \text{concretize}(\boldsymbol{W}_{t}, \gamma)$ 7: $\boldsymbol{\epsilon} \leftarrow [\boldsymbol{\epsilon}_{\boldsymbol{x}}^{\top}, \boldsymbol{\epsilon}_{\boldsymbol{\mu}}^{\top}, \Delta \boldsymbol{\mu}^{\top}, \gamma \Delta \boldsymbol{\sigma}^{\top}]^{\top}$ 8: $\boldsymbol{z}_{t} \leftarrow [\hat{\boldsymbol{x}}_{t}^{\top}, \hat{\boldsymbol{\mu}}_{t}^{\top}, \mathbf{0}_{6}^{\top}, \mathbf{0}_{6}^{\top}]^{\top}$ 9: $\overline{\mathcal{R}}_{t}' \leftarrow \mathcal{B}(\boldsymbol{z}_{t}, \boldsymbol{\epsilon})$ 10: for i in $\{t+1, \ldots t+\tau_{r}\}$ do

- $\overline{\mathcal{R}}_i' \leftarrow \mathtt{jax_verify}(\overline{G_{cl}}, \, \overline{\mathcal{R}}_{i-1}')$
- $\overline{\mathcal{R}_{\underline{i}}} \! \leftarrow \! \mathtt{projection}(\overline{\mathcal{R}}_{i}')$
- if $\overline{\mathcal{R}}_i \cap \mathcal{C} \neq \emptyset$ then
- $c \leftarrow \text{false}$
- end if
- 16: end for
- 17: **return** c

At each time step, $y_{t-\tau_e:t}$ is measured by the on-board sensors and passed to the MHE, which determines optimal values for $\hat{x}_{t-\tau_e:t}$ and $\hat{w}_{t-\tau_e:t}$. Using the output from the MHE, we determine estimates for the state \hat{x}_t and its covariance $Q_{t|t-1}$, as well as disturbance parameter estimates $\hat{\mu}_t$ and \hat{W}_t . On lines 5 and 6 we then obtain concrete uncertainty bounds ϵ by truncating the normal distribution according to concretization parameter γ . Next we construct the set of possible inputs for G_{cl} . On lines 7, 8, and 9 the possible states $\mathcal{B}(\hat{x}_t, \epsilon_x)$, noise values $\mathcal{B}(\hat{\mu}_t, \epsilon_\mu)$, and reachability variables $\mathcal{B}(\mathbf{0}_6, [\Delta \mu^\top, \Delta \sigma^\top]^\top)$, are concatenated to get the initial set $\overline{\mathcal{R}}_t'$ necessary for reachability analysis. Next, on lines 10 and 11 we loop over the horizon τ_r , calculating RSOAs for each time step. Notice that the RSOA is the set of possible states and disturbance terms, $\overline{\mathcal{R}}_t' \subset \mathbb{R}^{4n_x}$. Thus, on line 12, we project $\overline{\mathcal{R}}_t'$ onto \mathbb{R}^{n_x} , thereby enabling us to check the safety condition on 13, which is the desired result.

5.3.3 Formal Analysis

Theorem 5.2 formally states the results of our approach. The full proof of the theorem is outlined in (Rober et al., 2024). For continuity with the presentation in this paper we use a system state $x_t \in \mathbb{R}^6$, but the same results can be extended to higher order systems.

Theorem 5.2 (Safety Verification for an Uncertain System). Consider a system (6) subject to a disturbance $\mathbf{w}_t \sim \mathcal{N}(\boldsymbol{\mu}_t, \mathbf{W}_t)$ truncated at γ standard deviations, where $\boldsymbol{\mu}_t$ and \mathbf{W}_t satisfy the assumptions specified by (7) and where $\hat{\boldsymbol{\mu}}_t$ and $\hat{\mathbf{W}}_t$ are accurate estimates for their respective parameters at the current time step. The iterative application of Theorem 5.1 with \mathbf{G}_{cl} defined by Eqs. (38) to (41) and where $\mathcal{I} = \mathcal{B}_{\infty}(\mathbf{z}_t, \boldsymbol{\epsilon})$, $\boldsymbol{\epsilon} = [\boldsymbol{\epsilon}_{\boldsymbol{x}}^{\top}, \boldsymbol{\epsilon}_{\boldsymbol{\mu}}^{\top}, \Delta \boldsymbol{\mu}^{\top}, \gamma \Delta \boldsymbol{\sigma}^{\top}]^{\top}$ and $\mathbf{z}_t = [\hat{\boldsymbol{x}}_t^{\top}, \hat{\boldsymbol{\mu}}_t^{\top}, \mathbf{0}_6^{\top}, \mathbf{0}_6^{\top}]^{\top}$ provides bounds on all possible $\hat{\boldsymbol{x}}_{t:t+\tau_r}$, i.e., $\overline{\mathcal{R}}_{t:t+\tau_r}$.

6 Implementation Details

6.1 Speed Controller Details

The linearized speed dynamics, which were experimentally obtained by offline system identification, are

$$\dot{u}_{sog} = -24u_{sog} + 0.618\Lambda_1 \left(u_{thr} + \Delta_{u_{sog}} \left(u_{sog} \right) \right), \tag{42}$$

where $\Delta_{u_{sog}}(u_{sog}): \mathbb{R} \to \mathbb{R}$ represents an unknown parametric matched uncertainty. The parameters for baseline controller design were

$$Q_{u_{sog}} = \begin{bmatrix} 150 & 0 \\ 0 & 1 \end{bmatrix}, \quad \text{and} \quad R_{u_{sog}} = 2$$

$$\tag{43}$$

The controller was implemented at 10 Hz. The resulting PI gains were

$$k_{u,p} = 0.36556$$
 and $k_{u,i} = 8.6603$. (44)

The discrete time controller and integrator are

$$u_{thr}(t) = k_{u,p}u(t) + k_{u,i}e_{uI}(t),$$
 (45)

$$e_{uI}(t+1) = e_{uI}(t) + (u(t) - u_d) \Delta t.$$
 (46)

The integral component in (46) is bounded using the anti-windup logic in (Åström and Hägglund, 2006, Sec.3.5) with $k_{u,aw} = 0.1407$. The regression vector $\Phi(u_{sog})$ in the adaptive controller was implemented with a bias term and radial basis functions (RBFs) (Lavretsky and Wise, 2012, Eq. 12.6). Specifically, 11 RBFs were placed in the speed dimension centered at speed values of $\{0.5, 0.6, ..., 1.4, 1.5\}$ meters per second. The adaptive update laws were implemented with linear deadzone operators (Lavretsky and Wise, 2012, Eq. 11.19) and a rectangular projection operator (Lavretsky and Wise, 2012, Pg. 352).

6.2 Yaw-Rate Controller Details

The linearized sway-yaw rate dynamics, which were experimentally obtained by offline system identification, are

$$\begin{bmatrix} \dot{v} \\ \dot{r} \end{bmatrix} = \begin{bmatrix} -0.023 & -0.0075 \\ 0 & -61 \end{bmatrix} \begin{bmatrix} v \\ r \end{bmatrix} + \begin{bmatrix} -0.0009 \\ 0.90 \end{bmatrix} \Lambda_{p_2} \left(u_{rud} + \Delta_r \left(r \right) \right), \tag{47}$$

where $\Delta_r(r): \mathbb{R} \to \mathbb{R}$ represents an unknown parametric matched uncertainty. When estimating the system dynamics we found the entries in A_p and B_p the correspond to the sway dynamics to be small in magnitude but non-zero, even though the system is underactuated. Their inclusion does not directly impact the yaw-rate dynamics, and are reported for completeness. For yaw-rate tracking the, the LQR parameters are

$$Q_r = \begin{bmatrix} 100 & 0 & 0 \\ 0 & 10 & 0 \\ 0 & 0 & 10 \end{bmatrix}, \quad \text{and} \quad R_r = 0.01.$$
 (48)

The controller was implemented at 10 Hz. The resulting PI gains were

$$k_{v,p} = -0.33, \quad k_{r,p} = 8.44, \quad \text{and} \quad k_{r,i} = 100.$$
 (49)

The discrete time controller and integrator are

$$u_{rud}(t) = k_{v,p}v(t) + k_{r,p}r(t) + k_{r,i}e_{rI}(t)$$
(50)

$$e_{rI}(t+1) = e_{rI}(t) + (r(t) - r_d)\Delta t.$$
 (51)

The integral component in (51) is bounded using the anti-windup logic in (Åström and Hägglund, 2006, Sec.3.5) with $k_{r,aw}=1.1667$. Similar to the speed controller, the regression vector Φ in the adaptive controller was implemented with a bias term and RBFs (Lavretsky and Wise, 2012, Eq. 12.6). Specifically, 21 RBFs were placed in the yaw rate dimension centered at values of $\{-20, -18, ..., 18, 20\}$ degrees per second.

Finally, we report the constants used for the heading to yaw-rate controller which filters the output from pHelmIvP as described in Section 4.1.4. During experiments we used $\tau_u = 1s$, $\tau_r = 0.1$, and $\tau_\theta = 0.2$. During the UNREP experiment we decreased the size of domain intervals to $0.01 \frac{m}{s}$ for speed and $0.1 \frac{rad}{s}$ for heading.

6.3 Thruster Allocation

The output from the speed and heading controllers, u_{thr} and u_{rud} , is allocated to the left and right thruster of the Heron USV with the following thruster mixing equations:

$$u_L = u_{thr} * \left(1 + \frac{u_{rud}}{R_{max}}\right) \tag{52}$$

$$u_R = u_{thr} * \left(1 - \frac{u_{rud}}{R_{max}}\right) \tag{53}$$

 R_{max} is the maximum allowable rudder and was set at $R_{max} = 50$ for all field experiments.

6.4 Payload Autonomy

The system architecture follows the backseat driver design philosophy (Benjamin et al., 2010) with the following modification: All the control processes ran on the payload autonomy computer which then

sent the control inputs u_L and u_R to the front seat. A system

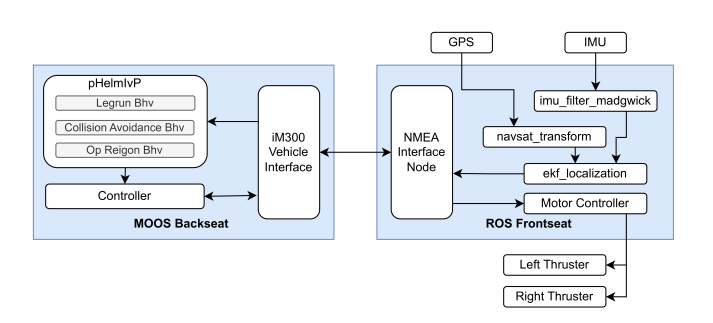


Figure 5: System architecture detailing backseat payload autonomy with commercial Heron frontseat.

A system overview is provided in Figure 5.

Table 1: Sensor and Process Rates.

Sensor or Process	Freq (Hz)
IMU	40
GPS	5
robot_localization ROS Package	
(Moore and Stouch, 2014)	20
Controller	20
HelmIvP	4 (10*)
Reachability Calculation	10

^{*}Rate was increased during UNREP experiments

As for the reachabilty calculation, the same architecture was simplified for speed of calculation. More specifically, the guidance input was not generated from the pHelmIvP multi-objective behavior optimization process, but instead it was calculated based on a trackline of a single dominant waypoint behavior. As a result, the reachability analysis is limited in the sense that it does not consider the multiple objectives of waypoint following, collision avoidance, and remaining inside the operational region. However, we found this simplification to be acceptable given the limited time horizon.

6.5 Timing

There were no guarantees of message timing because the system operated on two separate computers with two different middlewares: ROS and MOOS. Furthermore, the state estimation was shared over WiFi between vehicles during the UNREP experiment which resulted in additional time delays of signals used in the controller. During preliminary testing we observed propagation of time delays through the system that resulted in poor performance. These issues motivated a focus on increasing cycle frequency where possible and implementing processes that were robust to inconsistent message timing. A summary of the cycle frequencies can be found in Table 1.

7 Configuration of Field Experiments

Field experiments were conducted near the MIT Sailing Pavilion in Cambridge MA. The sailing pavilion provided access to the Charles River Basin, a public water space near the MIT campus. An overview of the operational area is shown in Figure 6. Development began in Febuary 2023 and continued until a final demonstration on November 19, 2023. Over 80 missions were conducted. The control approaches were developed and tested in a variety of weather and surface conditions during the eight month season. The experimental results reported herein were collected on the final day of testing, November 19th 2023. The air temperature for the day ranged from -0.6 °C to 3 °C and the wind speed varied from $2.2 \, m/s$ to $4.9 \, m/s$ as recorded by the MIT Sailing pavilion weather station.

7.1 Definition of Control Approaches Tested in the LegRun Mission

In every test we compared the performance of the MRAC controller to the existing proportional integral derivative (PID) baseline controller. Since the LegRun scenario offered a more structured and repeatable method of testing, we also compared performance of the MRAC controller to an LQR PI controller that did not have the adaptive term. Specifically the three controller used in testing were: For each experiment, we deployed one of the following controllers:

A baseline PID controller designed for the Heron USV by the manufacturer and members of the MIT PavLab.



Figure 6: Overview of operational area near the MIT sailing pavilion This controller has been in service on the aforementioned platform for approximately seven years.

- LQR PI as described in Section 4.2.1
- MRAC as described in Section 4.2.3

7.2 USV Disturbances

Our goal was to thoroughly test the performance of the controllers when the USV was subject to significant disturbances, or disturbances that are greater in magnitude than would be reasonable expected in operation. To that end we developed three disturbances: simulated thruster failure, a sail, and a drogue.

7.2.1 Simulated Thruster Failure

Significant changes to thruster performance of the Heron USV can occur for many reasons including a blocked inlet duct, a line wrapped around the propeller, or a blocked outlet duct. Since these real disturbances can cause permanent damage to the USV, the effect of thruster failure was simulated in software. The simulated failures were parameterized by multiplicative and additive bias terms that transform the intended commanded input into a "faulty" input.

Given the definition of these thruster failure modes:

- F_{rf} is the rudder fault multiplicative factor where $F_{rb} = 1$ is no disturbance
- F_{rb} is the rudder fault additive bias
- F_{tf} is the thruster fault multiplicative factor where $F_{tf} = 1$ is no disturbance
- F_{tb} is the thruster fault additive bias

the calculation of the "faulty" thruster commands is expressed as

$$F_{rb_L} = \frac{F_{rf} - 1}{2} \cdot (u_L - u_R) \tag{54}$$

$$F_{rb_R} = \frac{F_{rf} - 1}{2} \cdot (u_R - u_L) \tag{55}$$

$$\tilde{u}_L = u_L \cdot F_{tf_L} + F_{tb_L} + F_{rb_L} \tag{56}$$

$$\tilde{u}_R = u_R \cdot F_{tf_R} + F_{tb_R} + F_{rb_R},\tag{57}$$

where u_L and u_R are the intended inputs. The faulty commands \tilde{u}_L and \tilde{u}_R are sent to the front-seat motor controller instead of the intended commands.

7.2.2 Sail

The sail deployed remotely when given a command from either a shore side operator, or at a pre-programmed location along the mission. The sail deployment is shown in Figure 7a and Figure 7b. The sheet attached to the free end of the boom was connected to the back end of the Heron and remained constant length. As a result the boom traveled to a position that was almost perpendicular to the body center-line when the sail was engaged. The sail was mounted approximately halfway back on the port side and was free to rotate to either side in response to wind. As a result of the offset positioning, the sail could induce greater moments in the positive Z direction.





- (a) The sail secured in a stowed position at the start of the mission.
- (b) The sail was deployed remotely during the mission.

Figure 7: Remotely deployed sail disturbance.

7.2.3 Drogue

Similar to the sail, the drogue deployed remotely when given a command from either a shore side operator, or at a pre-programmed location along the mission. A five gallon bucket served as the main component of the drogue and was attached to the body of the Heron with two ropes. The bucket was mounted to the back of the Heron, and when the deployment command was received the bucket passively fell off the body into the water behind the vehicle. The deployment process is shown in Figure 8a and Figure 8b.



(a) Drogue secured on the rear of the Heron at the start of the mission.



(b) Drogue was deployed remotely during the mission and pulled through the water behind the USV.

Figure 8: Remotely deployed drogue (bucket) disturbance.

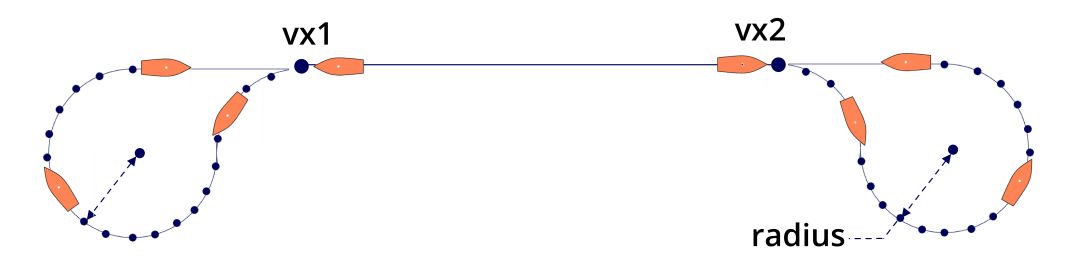


Figure 9: Overview of LegRun behavior used in experimental testing. Each LegRun path is parameterized by a radius and two waypoints, vx1 and vx2.

7.3 LegRun Evaluation Mission

The LegRun behavior is designed to facilitate the testing of a marine robotic platform by enabling the vehicle to traverse back and forth over a "legrun" trackline prescribed by two vertices. After reaching the end of the trackline, the vehicle switches into a Williamson turn mode to ensure vehicle alignment with the trackline when starting in the other direction. An overview of the intended action is shown in Figure 9.

The LegRun missions presented in this work starts with a sequence of two Williamson turns each of radius 20m followed by two tighter turns with radius 10m. In several ways the LegRun behavior is ideal for testing marine vehicles. By alternating direction of travel along the middle leg sections we ensure that the vehicle is subject to wind and wave forces from opposite directions. The behavior includes Williamson turns in both the left and right directions. As a practical matter, the behavior publishes a status of progress along the track and that was used to consistently trigger actuation of disturbances.

The LegRun behavior generates a sequence of waypoints that parameterize the entire path. At each iteration of pHelmIvP the behavior produces an objective function that maps the set of possible combinations of actions for speed and heading to utility. When multiple behaviors are active, the IvP optimizer in pHelmIvP determines the set of actions that maximize the sum of the utility functions of all active behaviors. More details can be found in (Benjamin et al., 2010).

During this portion of the field testing the LegRun behavior was almost always the sole active behavior, since the main objective was trackline following and there were no other vehicles to consider. Other behaviors usually remained idle, such as those related to safety, e.g. avoidColregs behavior, which implements collision avoidance in compliance with the naval COLREGS, and the opRegionBehavior which implements a containment region for the vehicle operations (Benjamin, 2024). As a result the pHelmIvp generated a desired reference that reflected the desired action selection from the LegRun behavior.

7.4 Straight Trackline Mission

In these missions the desired behavior of the Heron USV was to follow a relatively long, straight trackline. The intent of this mission was to validate the change in forward reachable sets as the USV transitions from a steady-state normal operating condition to a faulty condition. The straight line test offers a method to clearly evaluate the performance of the thruster bias estimation because it eliminates some of the complications found in the more involved LegRun mission, such as integrator wind-up in the alternating turns.

8 Experimental Results - Systematic Evaluation of Control and Forward Reachability Analysis

This section reports the performance of the adaptive control and real-time forward reachability analysis module in a set of systematic field experiments. The configuration details of these experiments is described in Section 7. Specifically,

we evaluated the performance of the MRAC controller against the LQR PI and PID controllers in the LegRun mission scenario. During several straight trackline missions the forward reachable sets were calculated in real-time throughout the mission, and this demonstrated the effectiveness of the bias estimation to capture the effect of significant disturbances on the reachable states. Discussion of the results is included at the end of the section.

8.1 LegRun Missions for Evaluation of Control Performance

In this section we report a sequence of tests that began with the USV completing the LegRun mission encumbered by only the naturally occurring disturbances from wind and waves. After a baseline was established, we repeated the same mission three times, each with a different significant disturbance as described in Section 7.2.

8.1.1 Baseline LegRun Mission

A series of experiments summarized in Fig. 10 show the performance of the PID, LQR PI, and MRAC controllers using the LegRun behavior with only naturally-occurring disturbances such as wind, waves, and river current. The trajectory and state error plots are reported in Fig. 10a and Fig. 10b respectively. Table 2 reports the speed, heading, yaw rate, and position error for the three controllers during the LegRun experiment.

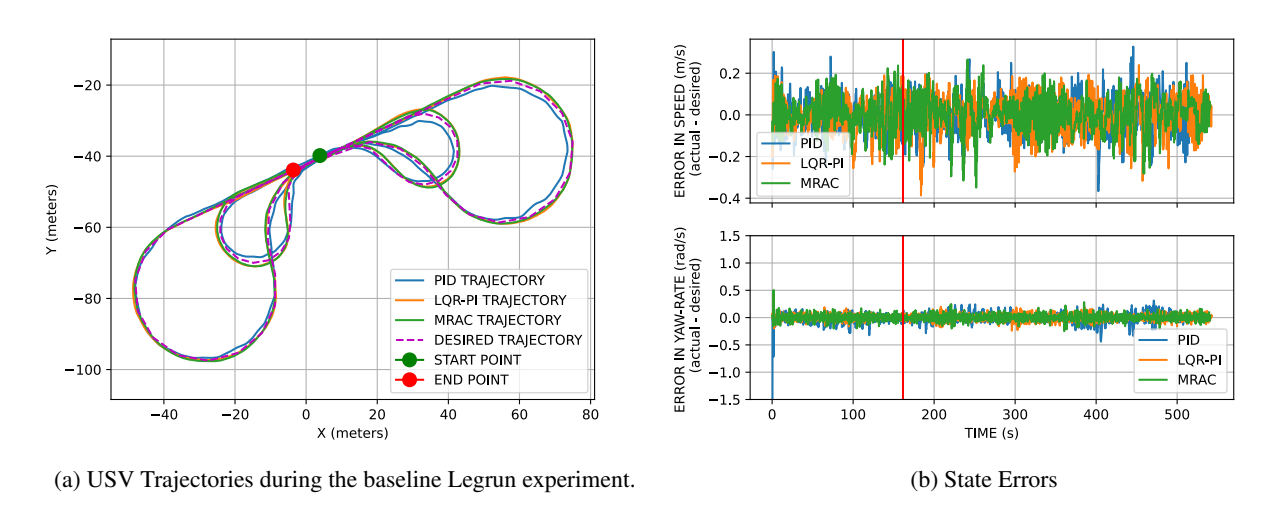


Figure 10: **Baseline** LegRun mission results. The Heron USV used the baseline track-line following algorithm (Section 4.1.1) with PID, LQR PI, MRAC inner loop controllers.

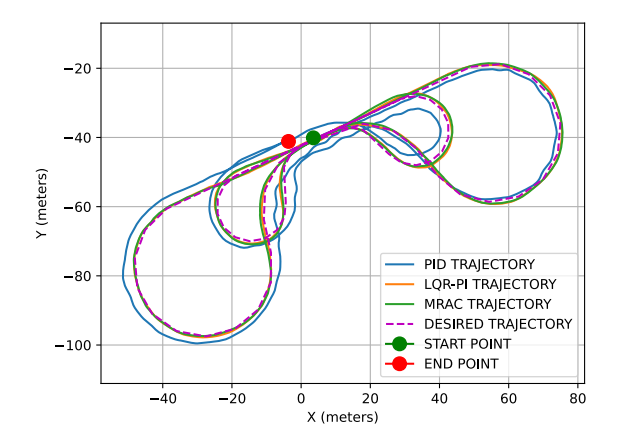
Table 2: Error Statistics (root mean squared error (RMSE) \pm root mean squared deviation (RMSD)) for the **Baseline** LegRun mission.

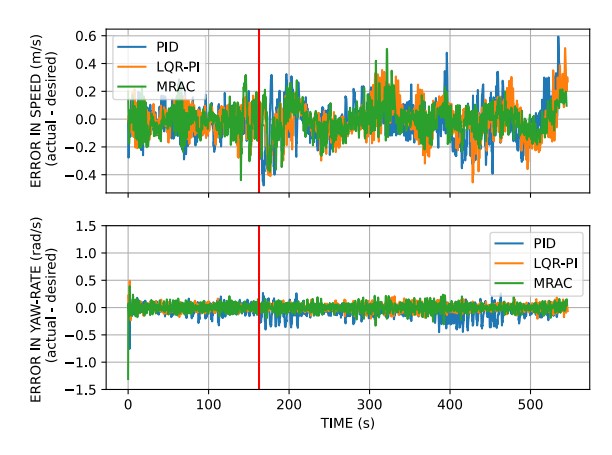
	PID	LQR-PI	MRAC
Speed Error (m/s)	0.09 ± 0.06	0.09 ± 0.06	$\textbf{0.08} \pm \textbf{0.06}$
Heading Error (deg)	$\textbf{10.35} \pm \textbf{7.34}$	17.63 ± 11.4	17.47 ± 11.40
Yaw Rate Error (rad/s)	0.09 ± 0.07	$\textbf{0.06} \pm \textbf{0.04}$	$\textbf{0.06} \pm \textbf{0.04}$
Position Error (m)	0.94 ± 0.57	0.47 ± 0.35	$\textbf{0.45} \pm \textbf{0.33}$

8.1.2 LegRun Mission with Simulated Fault

In the next series of experiments, we tested the PID, LQR PI, and MRAC controllers on the LegRun behavior with the natural disturbances and a reduction in the output of the left thruster by 50% of the commanded value, i.e. $F_{tfL} = 0.5$

in (56). The simulated fault was induced after the Heron completed the first large right loop of the LegRun. The results of these experiments are shown in Fig. 11 and Table 3. The trajectory and state error plots are reported in Fig. 11a and Fig. 11b respectively. Table 3 reports the speed, heading, yaw rate, and position error for the three controllers during the LegRun experiment with the simulated fault.





(a) USV Trajectories during the LegRun experiment with simulated 50% fault on the left thruster.

(b) State Errors

Figure 11: LegRun mission with **simulated thruster fault**. The Heron USV used the baseline track-line following algorithm (Section 4.1.1) with PID, LQR, MRAC inner loop controllers. The simulated fault was induced after the Heron completed the first large right loop of the LegRun.

Table 3: Error Statistics (RMSE \pm RMSD) for the LegRun mission with simulated thruster fault

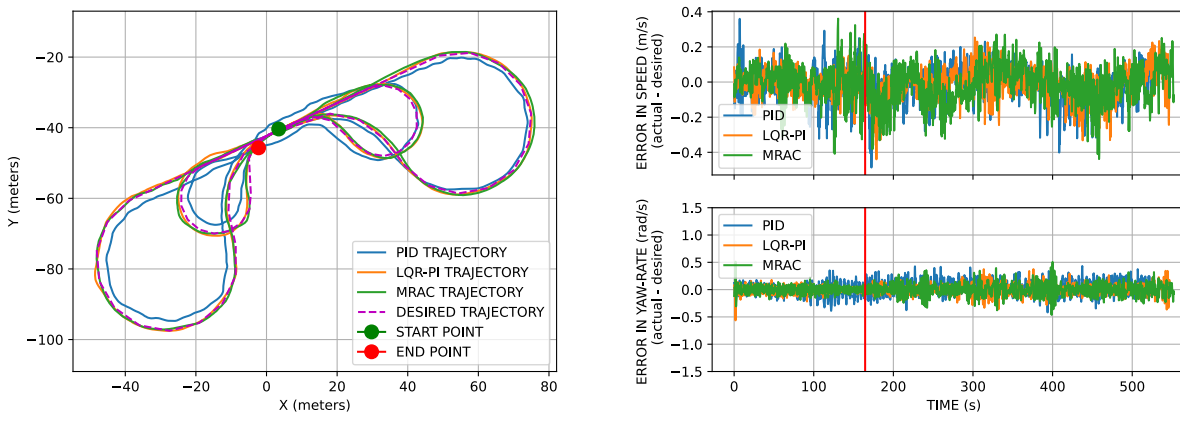
	PID	LQR-PI	MRAC
Speed Error (m/s)	0.14 ± 0.10	0.13 ± 0.09	$\textbf{0.11} \pm \textbf{0.07}$
Heading Error (deg)	27.73 ± 11.33	$\textbf{17.54} \pm \textbf{10.99}$	17.63 ± 11.00
Yaw Rate Error (rad/s)	0.14 ± 0.10	$\textbf{0.06} \pm \textbf{0.04}$	0.07 ± 0.05
Position Error (m)	2.54 ± 0.72	$\textbf{0.45} \pm \textbf{0.30}$	0.49 ± 0.31

8.1.3 LegRun Mission with Deployed Drogue

In this series of experiments, we tested the PID, LQR PI, and MRAC controllers on the LegRun behavior with the drogue, which was deployed after the Heron completed the first large right loop of the LegRun. The results of these experiments are shown in Fig. 12 and Table 4. The trajectory and state error plots are reported in Fig. 12a and Fig. 12b respectively. Table 4 reports the speed, heading, yaw rate, and position error for the three controllers during the LegRun experiment with the drogue deployed.

Table 4: Error Statistics (RMSE \pm RMSD) for the LegRun mission with **drogue fault**.

	PID	LQR-PI	MRAC
Speed Error (m/s)	0.10 ± 0.07	$\textbf{0.09} \pm \textbf{0.07}$	0.11 ± 0.07
Heading Error (deg)	19.02 ± 9.70	18.01 ± 11.37	$\textbf{17.76} \pm \textbf{10.97}$
Yaw Rate Error (rad/s)	0.14 ± 0.08	$\textbf{0.09} \pm \textbf{0.07}$	0.11 ± 0.08
Position Error (m)	1.89 ± 1.00	0.57 ± 0.57	$\textbf{0.43} \pm \textbf{0.39}$



(a) USV Trajectories during the LegRun experiment with drogue deployment.

(b) State Errors

Figure 12: LegRun mission with **drogue fault**. The Heron USV used the baseline track-line following algorithm (Section 4.1.1) with PID, LQR, MRAC inner loop controllers. The drogue was deployed after the Heron completed the first large right loop of the LegRun.

8.1.4 LegRun Mission with Deployed Sail

In this series of experiments, we tested the PID, LQR PI, and MRAC controllers on the LegRun behavior with the sail. The results of these experiments are shown in Fig. 13 and Table 5. The trajectory and state error plots are reported in Fig. 13a and Fig. 13b respectively. Table 5 reports the speed, heading, yaw rate, and position error for the three controllers during the LegRun experiment with the sail deployed.

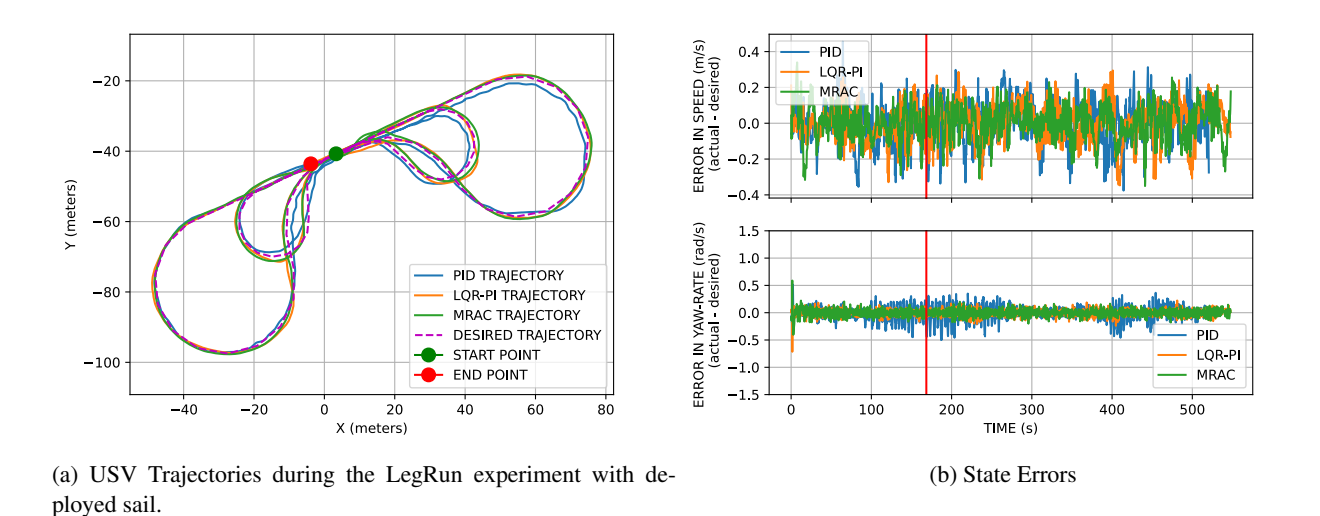


Figure 13: LegRun mission with **sail fault**. The Heron USV used the baseline track-line following algorithm (Section 4.1.1) with PID, LQR PI, MRAC inner loop controllers. The sail was deployed after the Heron completed the first large right loop of the LegRun.

Table 5: Error Statistics (RMSE \pm RMSD) for the LegRun mission with sail fault

	PID	LQR-PI	MRAC
Speed Error (m)	0.12 ± 0.08	$\textbf{0.06} \pm \textbf{0.04}$	0.09 ± 0.06
Heading Error (deg)	$\textbf{13.80} \pm \textbf{9.22}$	19.09 ± 12.67	18.04 ± 10.78
Yaw Rate Error (rad/s)	0.13 ± 0.10	$\textbf{0.06} \pm \textbf{0.04}$	$\textbf{0.06} \pm \textbf{0.04}$
Position Error (m)	1.07 ± 0.74	0.65 ± 0.47	$\textbf{0.59} \pm \textbf{0.41}$

8.2 Straight Trackline Missions for Evaluation of Forward Reachability Analysis

In this section we report the results from two experiments to validate the real-time calculation of forward reachable sets with bias estimation. We added unmodeled disturbances during the course of these experiments to highlight the change in forward reachable set. These significant disturbances were triggered approximately midway through the mission and after the USV had approximately achieved steady tracking of the straight reference trajectory. The configuration of the experiments is described in Section 7.4.

8.2.1 Straight Trackline Mission with Simulated Fault

In the first reachability experiment, shown in Fig. 14, the USV tracked along a straight line at $1.0^m/s$ until we induced a simulated thruster fault with $F_{tf_L} = F_{tf_L} = 0.3$ in (56).

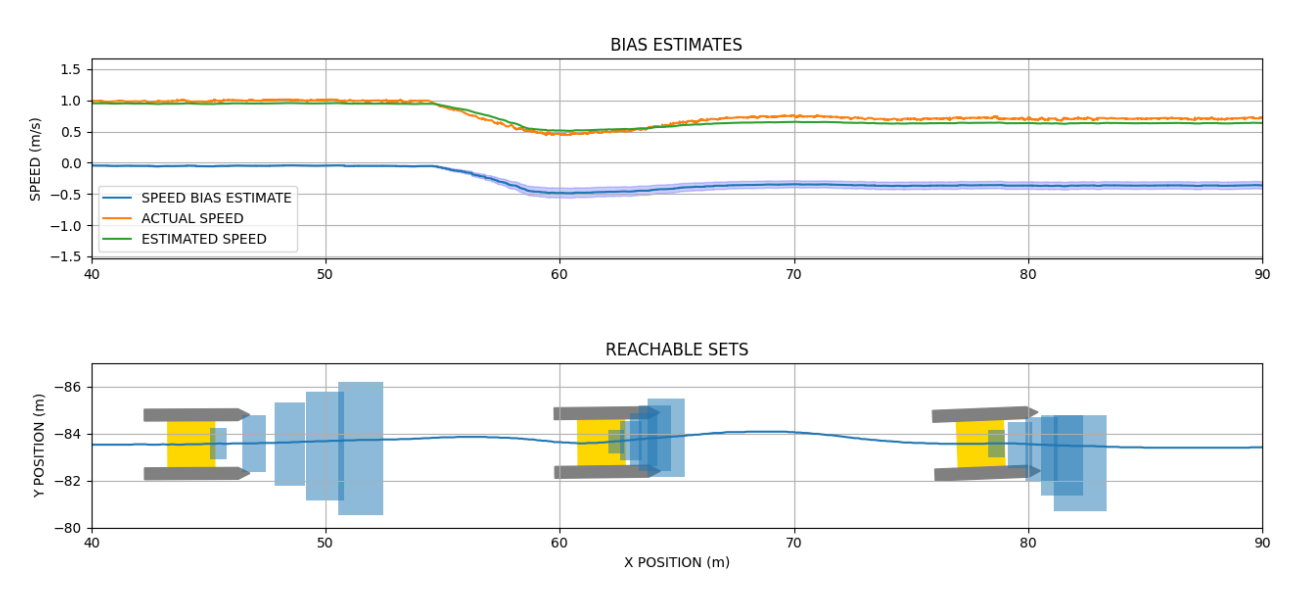


Figure 14: USV real-time forward reachability computation during the straight trackline mission with simulated fault on both thrusters where the input was reduced to 30% of the commanded value. The simulated disturbance occurs when the vehicle is approximately 55 meters along the x axis.

8.2.2 Straight Trackline Mission with Deployed Drogue

In the reachability experiment shown in Fig. 15, the USV tracked along a straight line at $1.0^m/s$ until we deployed a drogue to induce drag and reduce the vehicle speed.

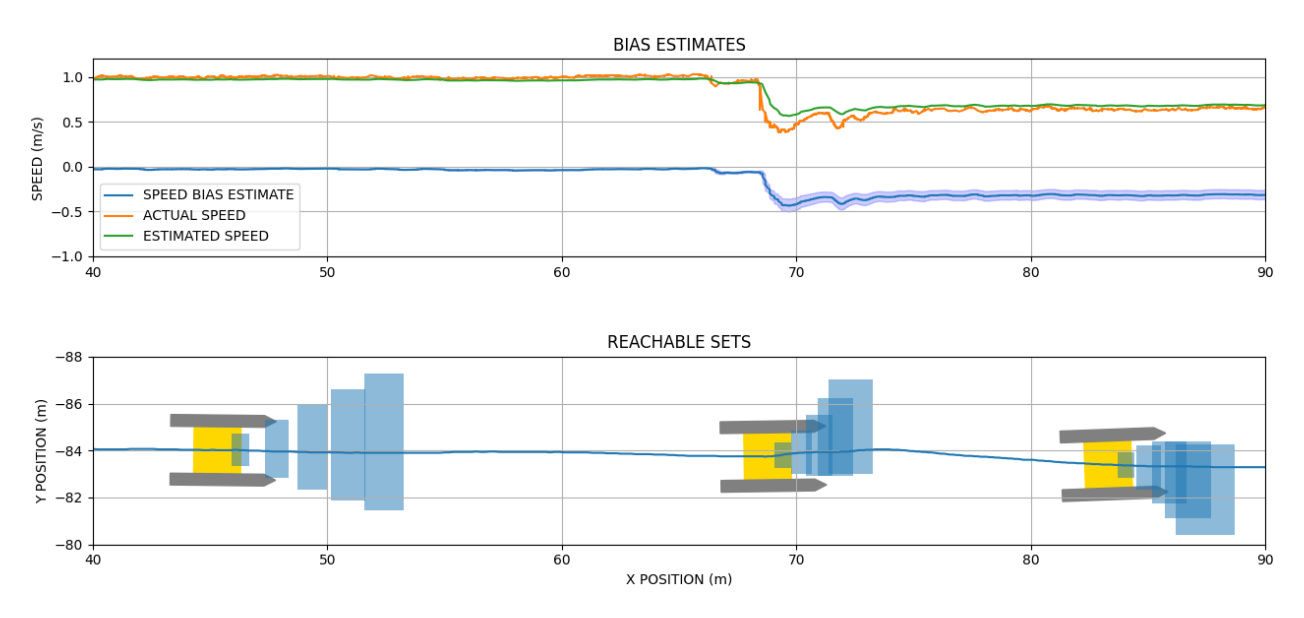


Figure 15: USV real-time forward reachability computation during the straight trackline mission with deployed drogue. The simulated disturbance occurs when the vehicle is approximately 66 meters along the x axis.

8.3 Discussion

We validated the performance of the controllers and forward reachability calculations on the USV in systematic and isolated tests. With the exception of heading error, the LQR PI and MRAC controllers performed better than the base-line PID. The most notable improvement was with regard to position error in all scenarios, and the percentage reduction in RMSE is listed in Table 6.

Table 6: Percentage improvement in RMSE for position

	Error reduction	Error reduction
Scenario	using LQR-PI	using MRAC
Baseline	50%	52%
Simulated Thruster Fault	82%	81%
Drogue Fault	70%	77 %
Sail Fault	39%	45%

We found more mixed results when comparing between the LQR PI and MRAC controllers as the differences in performance where much smaller. As shown in Table 6, the MRAC controller, which is an the adaptive augmentation of the LQR-PI controller, had slightly better performance on the basis of position error in three of the four scenarios, and similar performance in the simulated thruster fault scenario. These results are evidence that including adaptive augmentation, such as in our MRAC formulation, reduces error in position even when the underlying controller includes an integration term. In many situations, the position error is of the utmost importance and in the following section we use two real-world scenarios that further illustrate this point.

9 Experimental Results - Safety-Critical Scenarios

This section describes the experimental results in two scenarios were precise control of a marine vehicle and safety assurances are necessary: an UNREP scenario with two vehicles, and the transit through a narrow canal. There were two tests in each scenario: one where PID control is used, and the other where MRAC is used.

As described previously, these types of scenarios are barriers to fielding fully autonomous USVs because they are difficult to complete and in many cases there are no good alternatives. Even though they are hazardous, canals save significant time and energy. Tight passages similar to canals are also found in many harbors and inter-coastal waterways. Moreover, all vessels must depart from a pier or other structure which are usually located within a harbor, and while some crewed vessels use tugboats to carefully maneuver through a harbor, they often complete a portion of the passage out to open water under their own power. Resupplying in the open water is also challenging, but it can significantly extend the operational use of vessels since they do not need to return to a harbor to do it. The process of maneuvering close enough to another vessel to transfer supplies is complicated by the fact that most vessels are underactuated and lack a dynamic positioning system (DPS). As a result, the standard UNREP scenario in the open water involves both vehicles moving forward at a steady speed and then gradually closing the distance between them to connect cables. The alternative of physically joining the vehicles can lead to significant damage.

9.1 UNREP Scenario

In the UNREP scenario, two Heron USVs are tasked to safely perform a maneuver where the two vehicles cooperatively move in close proximity to each other. One Heron USV is a guide ship, and the other Heron USV is the approach ship. The guide ship is tasked with a straight line path following task, and the approach ship must reach a position that is a user selected distance to the port or starboard side of the guide ship. In these experiments the approaching Heron USV follows a behavior that uses the guidance law from (Skejic et al., 2009) as reported in Section 4.1.3. It is assumed that the vehicles can communicate state information freely between each other. A notable challenge when

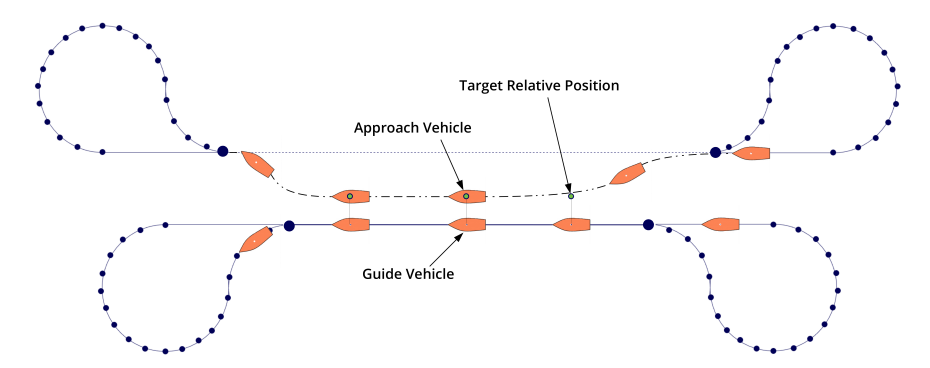


Figure 16: The UNREP test scenario is built upon two LegRun behaviors. When the guide vehicle enters the straight leg the UNREP process begins, and the UNREP approach behavior (Section 4.1.3) becomes active on the approaching vehicle. The approaching vehicle tracks a target position relative to the guide vehicle until the end of the straight leg. At the end of the leg both vehicles turn around and the process repeats in the opposite direction.

performing UNREP operations with full-scale models is the presence of a hull wash effect that can cause a net force in the sway degree-of-freedom that pushes the two vessels together as shown in Figure 17. This effect is difficult to model, and typically occurs with slender hydrodynamic bodies near each other (Reeve, 1911; Zhou et al., 2023). The body of the Heron USV is not large enough to produce a realistic hull wash effect; hence, a proximity-based thruster bias, which is not measured by the controller, was implemented to simulate hull wash effect for these experiments. Since the Heron USV is not directly actuated in the surge degree-of-freedom, the net effect was injected as a rotational bias on the two thrusters, i.e. in (56) and (57), $F_{tb_L} = F_{hw}$ and $F_{tb_R} = -F_{hw}$. The simulated hull wash disturbance F_{hw} for each USV was a function of the x and y separation distances in meters, s_{sep_x} and s_{sep_y} , with respect to the other USV's local coordinate frame. The hull wash disturbance was defined as

$$F_{hw} = \begin{cases} 0, & \text{if } s_{sep_x} > 15, s_{sep_y} > 15\\ \delta F_{hw_{max}} (1 - \frac{s_{sep_x}}{15}) (1 - \frac{s_{sep_y}}{15}), & \text{if } s_{sep_x} <= 15, s_{sep_y} <= 15 \end{cases}$$
(58)

The maximum simulated hull wash disturbance $F_{hw_{max}}$ was set to 20 for the UNREP missions. Additionally, the hull wash disturbance was applied when s_{sep_x} or s_{sep_y} were within 15 meters. The δ term defines the direction of the

rotational bias and is either 1 or -1 according to the heading of the other vehicle. This value is found by taking the sign of the outer product between the heading of the two vessels.

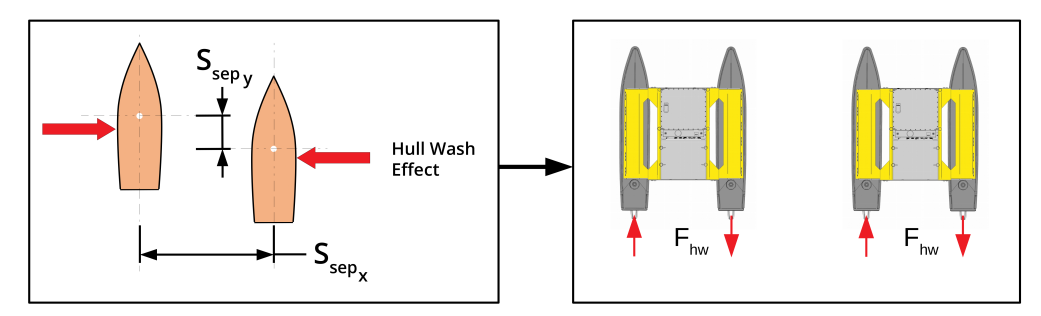
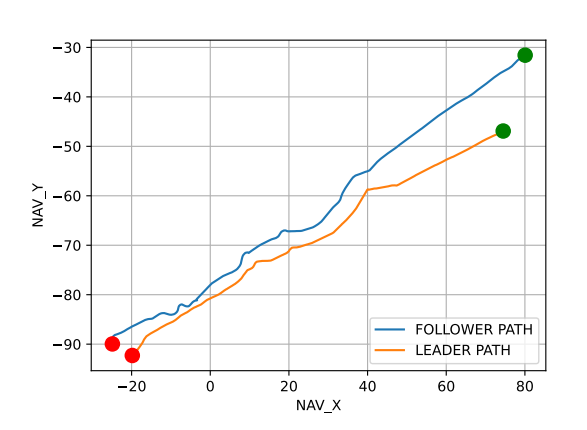
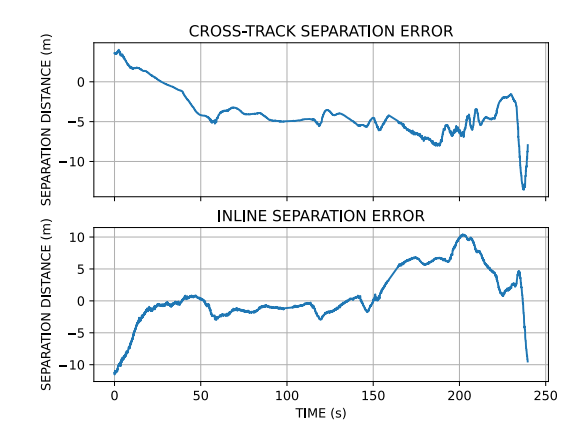


Figure 17: The simulated hull effect forces on each vehicle in the UNREP scenario where implemented as a rotational bias from the two thrusters per (58).

To add further uncertainty to the experiments, the drogue was deployed from the approach vessel shortly after the vehicle achieved relative position. Furthermore, both the guide and approach vessels faced a sudden 50% reduction in left thruster control effectiveness, $F_{tf_L} = 0.5$ in (56).





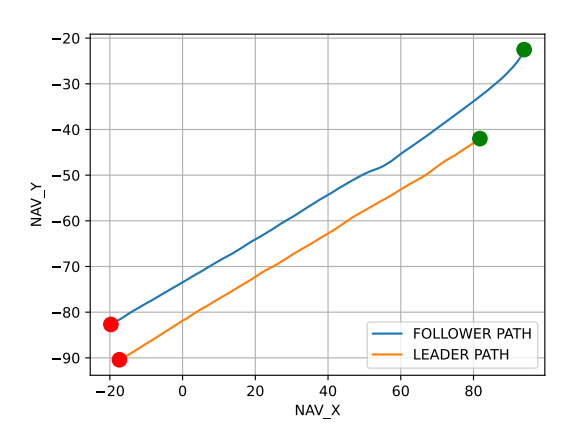
- (a) Trajectories with both vehicles under PID control.
- (b) Cross-track and inline separation errors with PID controller

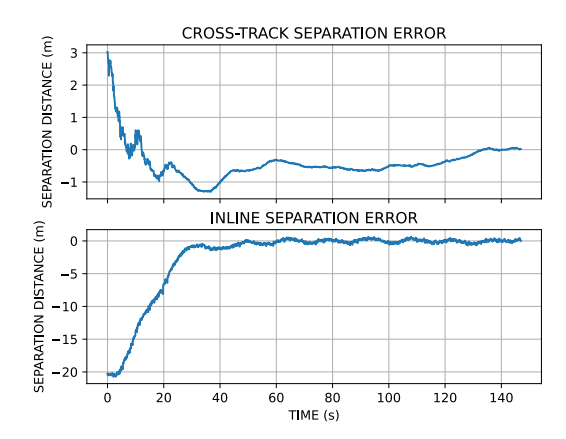
Figure 18: Experimental results for UNREP Scenario with PID controller

The results from two experimental trials are shown in Figure 18 and Figure 19. Despite the simulated hull wash effect, thruster reduction in effectiveness, and drogue device, both vessels completed the UNREP mission while using the developed MRAC controllers. However, the PID controller could not compensate for the uncertainty due to simulated hull wash effect alone; the PID controller failed and triggered an emergency vessel collision avoidance behavior before the thurster and drogue effects could be deployed. As expected, the MRAC controllers performed better than the PID controllers did in the UNREP scenario; MRAC has better error tracking and ability to reconstitute control despite the additional effects from this experiment.

9.2 Canal Scenario

The canal scenario was inspired by the 2021 Suez Canal obstruction incident where a ship ran aground due in part to additional wind loading and bank effect (Fan et al., 2022). In this experiment, one Heron USV was tasked to perform straight line-following through a virtual canal 8 meters wide where a bank effect was simulated when the vehicle deviates from the canal centerline. The virtual canal has a deadzone in the center where there is no simulated bank effect; however, outside of the deadzone but inside of the canal, the Heron USV was subject to a thruster bias that pointed the Heron USV away from the centerline and toward the "shore" of the virtual canal. The details of this effect





- (a) Trajectories with both vehicles under MRAC control.
- (b) Cross-track and inline separation errors with MRAC controller

Figure 19: Experimental results for UNREP Scenario with MRAC controller are shown in Figure 20. The implementation of this bank effect disturbance was identical in implementation of the

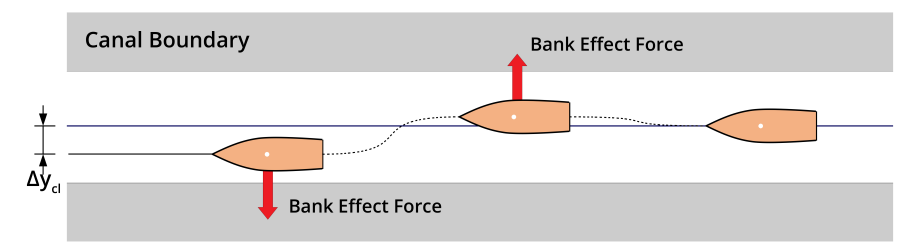


Figure 20: The canal transit scenario with simulated bank effect when the vehicle body approaches the edge of the canal.

hull effect disturbance from Section 9.1. Specifically, the value of the of simulated bank effect disturbance F_{be} as a function of the deviation from centerline Δy_{cl} was defined as

$$F_{be} = \begin{cases} 0, & \text{if } \Delta y_{cl} < w_d/2 \\ \delta(F_{be_{max}} - F_{be_{min}})(1 - \frac{w_c/2 - \Delta y_{cl}}{(w_c - w_d)/2}) + F_{be_{min}}, & \text{if } w_d/2 <= \Delta y_{cl} < w_c/2 \\ -99, & \text{if } \Delta y_{cl} >= w_c/2. \end{cases}$$
(59)

The width of the canal w_d for the mission was 8 meters. If the USV ever exits the canal boundary then a -99 bias is applied to both thrusters, effectively halting the USV. Note that the sign changes to F_{tb_L} and F_{tb_R} discussed for the hull wash disturbance are not applied when the ship exceeds the canal boundary. Additionally, the deadzone width for the canal w_c is 1 meter. The deadzone of the canal is the area near the centerline of the canal where no simulated disturbance is induced. The disturbance increases linearly from $F_{be_{min}}$ to $F_{be_{max}}$ when Δy_{cl} is between $w_d/2$ and $w_c/2$. $F_{be_{min}}$ and $F_{be_{max}}$ are 3 and 20 respectively for the canal mission. Similar to the UNREP case, the δ term is either 1 or -1 and defines the direction of the rotational bias by taking the sign of the outer product between the heading of the USV and the canal boundaries.

Furthermore, the vessel was subject to a sudden 50% reduction in control effectiveness of the left thruster and the deployable sail to increase environmental wind loading. To follow the trackline the Heron USV used the L_1 guidance behavior described in Section 4.1.2.

The experimental results from the canal scenario missions are shown in Figure 21. Despite the presence of the additional disturbances, the Heron USV with MRAC controller successfully navigated through the virtual canal, while it could not do so with the PID controller. The results from the two tests are shown in Figure 21. While the PID controller

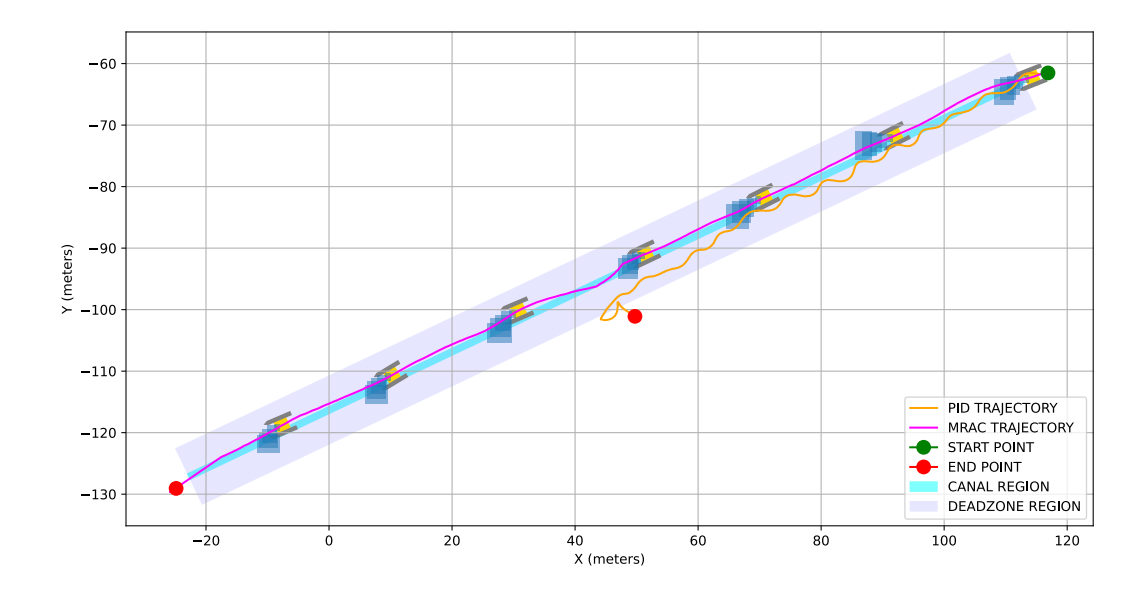


Figure 21: Trajectories of the Heron USV in the simulated canal with both PID and MRAC controllers. Approximately half-way along the canal the sail was deployed (at $x \approx 70m$) and the simulated thruster failure was commanded. The MRAC controller recovered and completed the mission, while the PID control did not. The forward reachable sets for the closed-loop system with the MRAC controller are shown in blue

attempted to recover, it was not able to correctly compensate for the additional uncertainty, causing the vehicle to "run aground" on the shore of the virtual canal. The MRAC controller quickly reconstituted control despite the effects of the three induced disturbances (simulated hull wash, thruster failure, and deployed sail) and naturally occurring disturbances (e.g., waves and river currents). Furthermore, the real-time reachable sets (shown in blue) reflected the change in the system dynamics that occurs at $x \approx 70m$. Just after the sail is deployed the size of the reachable sets decreases and they do not extend as far ahead of the USV. As the USV traveled further down the virtual canal we see the integration and adaptation in the MRAC controller take effect as the size of the reachable sets increase and their location extend further ahead of the USV, although neither fully recover to there original state.

10 Conclusions

This paper presented algorithms to provide control and safety verification to a USV subject to strong environmental disturbances and actuator malfunctions. We outlined an adaptive control formulation designed to handle varying disturbances and conducted extensive experiments showing its ability to maintain control despite induced drag forces and thruster malfunctions. Moreover, to provide safety certification in the face of such disturbances we demonstrated our approach to computing forward reachable sets in real-time using a MHE with a CG representation of the closed loop system.

Our experimental tests were conducted in two sets. In the first set of experiments we investigated the performance of the MRAC controller vs PID and LQR-PI in a series of repeated missions. Both the LQR-PI and MRAC controllers had better performance than the baseline PID, and with one exception, the MRAC controller had the lowest position error. We found more mixed results when comparing between the LQR PI and MRAC controllers as the differences in performance where much smaller. As shown in Table 6, the MRAC controller, which is an the adaptive augmentation of the LQR-PI controller, had slightly better performance on the basis of position error in three of the four scenarios, and similar performance in the simulated thruster fault scenario. These results are evidence that including adaptive augmentation, such as that in our MRAC formulation, reduces error in position even when the underlying controller

includes an integration term. Finally, we also validated the performance of the real-time reachability calculation and showed it could capture the effect of significant disturbances when computing the forward reachable sets.

In the second set of experiments, we demonstrated the performance of both adaptive control and forward reachability in two safety critical scenarios: UNREP and a canal transit. Both scenarios included significant disturbances in an effort to represent the worst case that could happen, and bolster confidence that these maneuvers can be completed autonomously, or with human supervision in the future. In both cases, we found that a Heron USV using our MRAC controller was able to complete the mission while the established baseline PID controller failed. Overall, these results on both control performance and safety assurances via real-time reachability are encouraging. Both the systematic evaluation and scenario demonstration suggest that adaptive control and real-time reachability could help facilitate wider user of USVs in the field because of improved performance in the face of unanticipated disturbances and the ability to provide real-time assessment of safety.

11 Acknowledgements

This work was supported in part by the US Navy NIWC Atlantic Award N6523623C8011. This research was developed with funding from the Defense Advanced Research Projects Agency (DARPA). The views, opinions and/or findings expressed are those of the author(s) and should not be interpreted as representing the official views or policies of the Department of Defense or the U.S. Government.

References

- Allgöwer, F., Badgwell, T. A., Qin, J. S., Rawlings, J. B., and Wright, S. J. (1999). Nonlinear predictive control and moving horizon estimation—an introductory overview. *Adv. Control*, pages 391–449.
- Althoff, M. and Dolan, J. M. (2014). Online verification of automated road vehicles using reachability analysis. *IEEE Trans. Rob.*, 30(4):903–918.
- Antonelli, G., Chiaverini, S., Sarkar, N., and West, M. (2001). Adaptive control of an autonomous underwater vehicle: experimental results on ODIN. *EEE Trans. Control Syst. Technol.*, 9(5):756–765.
- Åström, K. J. and Hägglund, T. (2006). *Advanced PID control*. ISA-The Instrumentation, Systems and Automation Society.
- Bansal, S., Chen, M., Herbert, S., and Tomlin, C. J. (2017). Hamilton-jacobi reachability: A brief overview and recent advances. In *Proc. IEEE Conf. Decis. Control*, pages 2242–2253. IEEE.
- Benjamin, M. R. (2024). An overview of MOOS-IvP and a users guide to the IvP helm. https://oceanai.mit.edu/ivpman/pmwiki/pmwiki.php. Release 22.8.
- Benjamin, M. R., Schmidt, H., Newman, P. M., and Leonard, J. J. (2010). Nested autonomy for unmanned marine vehicles with MOOS-IvP. *J. Field Robotics*, 27(6):834–875.
- Bolender, M. A., Dauby, B., Muse, J. A., and Adamczak, D. (2015). Hifire 6: Overview and status update 2015. In 20th AIAA International Space Planes and Hypersonic Systems and Technologies Conference.
- Borrelli, F., Bemporad, A., and Morari, M. (2017). *Predictive Control for Linear and Hybrid Systems*. Cambridge University Press.
- Deepmind (2020). jax_verify: Neural network verification in jax.
- Dutta, S., Chen, X., and Sankaranarayanan, S. (2019). Reachability analysis for neural feedback systems using regressive polynomial rule inference. In *Proc. Int. Conf. Hybrid Syst.: Comp. Control*, pages 157–168.

- Dydek, Z. T., Annaswamy, A. M., and Lavretsky, E. (2013). Adaptive control of quadrotor UAVs: A design trade study with flight evaluations. *EEE Trans. Control Syst. Technol.*, 21(4):1400–1406.
- Evans, L. C. (1998). Graduate studies in mathematics, volume 19. American Mathematical Society Providence, RI.
- Everett, M., Habibi, G., and How, J. P. (2021a). Efficient reachability analysis of closed-loop systems with neural network controllers. In *Proc. IEEE Int. Conf. Robot. Autom.*, pages 4384–4390. IEEE.
- Everett, M., Habibi, G., Sun, C., and How, J. P. (2021b). Reachability analysis of neural feedback loops. *IEEE Access*, 9:163938–163953.
- Fan, J., Huang, C., Chen, X., Li, W., and Zhu, Q. (2020). ReachNN*: A tool for reachability analysis of neural-network controlled systems. In *Proc. Int. Symp. Autom. Tech. for Verif. Anal.*, pages 537–542. Springer.
- Fan, S., Yang, Z., Wang, J., and Marsland, J. (2022). Shipping accident analysis in restricted waters: Lesson from the Suez Canal blockage in 2021. *Ocean Eng.*, 266:113119.
- Fischer, N., Hughes, D., Walters, P., Schwartz, E. M., and Dixon, W. E. (2014). Nonlinear RISE-based control of an autonomous underwater vehicle. *IEEE Trans. Rob.*, 30(4):845–852.
- Fossen, T. (1994). Guidance and Control of Ocean Vehicles. Wiley.
- Fossen, T. and Fjellstad, O.-E. (1993). Cascaded adaptive control of marine vehicles with significant actuator dynamics. In *Proc. Int. Fed. Autom. Control*, volume 26, issue 2, part 4,, pages 1123–1128.
- Fossen, T. I. and Fjellstad, O.-E. (1995). Robust adaptive control of underwater vehicles: A comparative study. *Int. Fed. Autom. Control Proc. Vol.*, 28, issue 2:66–74. 3rd IFAC Workshop on Control Applications in Marine Systems, Trondheim, Norway, 10-12 May.
- Frittelli, J., Goldman, B., and Lohman, A. E. (2024). Baltimore bridge collapse: Frequently asked questions. Technical Report CRS Report No. R48028, Congressional Research Service, Washington DC, USA.
- Fukao, T., Nakagawa, H., and Adachi, N. (2000). Adaptive tracking control of a nonholonomic mobile robot. *IEEE Trans. Robot. Autom.*, 16(5):609–615.
- Gleason, J. D., Vinod, A. P., and Oishi, M. M. (2017). Underapproximation of reach-avoid sets for discrete-time stochastic systems via Lagrangian methods. In *Proc. IEEE Conf. Decis. Control*, pages 4283–4290. IEEE.
- Haldeman, C. D., Aragon, D. K., Miles, T., Glenn, S. M., and Ramos, A. G. (2016). Lessening biofouling on long-duration AUV flights: Behavior modifications and lessons learned. In *Proc. IEEE OCEANS*, pages 1–8. IEEE.
- Harris, Z. J., Mao, A. M., Paine, T. M., and Whitcomb, L. L. (2023). Stable nullspace adaptive parameter identification of 6 degree-of-freedom plant and actuator models for underactuated vehicles: Theory and experimental evaluation. *Int. J. Robot. Res.*, 42(12):1070–1093.
- Herbert, S. L., Chen, M., Han, S., Bansal, S., Fisac, J. F., and Tomlin, C. J. (2017). Fastrack: A modular framework for fast and guaranteed safe motion planning. In *Proc. IEEE Conf. Decis. Control*, pages 1517–1522. IEEE.
- Hu, H., Fazlyab, M., Morari, M., and Pappas, G. J. (2020). Reach-SDP: Reachability analysis of closed-loop systems with neural network controllers via semidefinite programming. In *Proc. IEEE Conf. Decis. Control*, pages 5929–5934. IEEE.
- Huang, C., Fan, J., Li, W., Chen, X., and Zhu, Q. (2019). ReachNN: Reachability analysis of neural-network controlled systems. *ACM Trans. Embed. Comp. Sys.*, 18(5s):1–22.
- Huang, W., Wang, K., Lv, Y., and Zhu, F. (2016). Autonomous vehicles testing methods review. In *Proc. IEEE Int. Conf. Intell. Trans. Syst.*, pages 163–168. IEEE.
- Ivanov, R., Weimer, J., Alur, R., Pappas, G. J., and Lee, I. (2019). Verisig: verifying safety properties of hybrid systems with neural network controllers. In *Proc. Int. Conf. Hybrid Syst.: Comp. Control*, pages 169–178.

- Katz, G., Huang, D. A., Ibeling, D., Julian, K., Lazarus, C., Lim, R., Shah, P., Thakoor, S., Wu, H., Zeljić, A., et al. (2019). The Marabou framework for verification and analysis of deep neural networks. In *Proc. Int. Conf. Comput. Aid. Verif.*, pages 443–452. Springer.
- Koopman, P. and Wagner, M. (2016). Challenges in autonomous vehicle testing and validation. *SAE Int. J. Transp. Saf.*, 4(1):15–24.
- Lavretsky, E. and Wise, K. A. (2012). Robust and adaptive control: With aerospace applications. Springer.
- Lee, J. and Wong, E. (2021). Suez canal blockage: an analysis of legal impact, risks and liabilities to the global supply chain. *MATEC Web. Conf.*, 339:01019.
- Lew, T. and Pavone, M. (2021). Sampling-based reachability analysis: A random set theory approach with adversarial sampling. In *Proc. Conf. Robot Learn.*, pages 2055–2070. PMLR.
- Liu, Z., Zhang, Y., Yuan, C., and Luo, J. (2021). Adaptive path following control of unmanned surface vehicles considering environmental disturbances and system constraints. *IEEE Trans. Syst., Man, Cybern.: Syst.*, 51(1):339–353.
- Makavita, C. D., Jayasinghe, S. G., Nguyen, H. D., and Ranmuthugala, D. (2020). Experimental comparison of two composite MRAC methods for UUV operations with low adaptation gains. *IEEE J. Ocean. Eng.*, 45(1):227–246.
- McFarland, C. J. and Whitcomb, L. L. (2014). Experimental evaluation of adaptive model-based control for underwater vehicles in the presence of unmodeled actuator dynamics. In *Proc. IEEE Int. Conf. Robot. Autom.*, pages 2893–2900.
- Miller, M. O., Hammett, J. W., and Murphy, T. P. (1987). The development of the US Navy underway replenishment fleet. *Soc. Naval Archit. Mar. Eng.-Trans.*, 95.
- Mitchell, I. M. (2007). Comparing forward and backward reachability as tools for safety analysis. In *Int. Workshop on Hybrid Sys.: Comp. Control*, pages 428–443. Springer.
- Moore, T. and Stouch, D. (2014). A generalized extended Kalman filter implementation for the robot operating system. In *Proc. Int. Conf. Intel. Auto. Sys.* Springer.
- Narendra, K. S. and Annaswamy, A. (2005). *Stable Adaptive Systems*. Dover Books on Electrical Engineering. Dover Publications.
- Narendra, K. S., Annaswamy, A. M., and Singh, R. P. (1985). A general approach to the stability analysis of adaptive systems. *Int. J. Control*, 41(1):193–216.
- Park, S., Deyst, J., and How, J. (2004). A new nonlinear guidance logic for trajectory tracking. In *Proc. AIAA Guid.*, *Nav., Control.*
- Pedrozo, R. (2023). Advent of a new era in naval warfare: Autonomous and unmanned systems. In *Autonomous Vessels in Maritime Affairs: Law and Governance Implications*, pages 63–80. Springer.
- Polvara, R., Sharma, S., Wan, J., Manning, A., and Sutton, R. (2018). Obstacle avoidance approaches for autonomous navigation of unmanned surface vehicles. *J. Nav.*, 71(1):241–256.
- Reeve, S. A. (1911). The hydraulic interaction between passing vessels, called "suction". In *Proc. United States Naval Inst.*, volume 37, pages 1347–1376.
- Rober, N., Hammond, M., Cichella, V., Martin, J. E., and Carrica, P. (2022). 3D path following and \mathcal{L}_1 adaptive control for underwater vehicles. *Ocean Eng.*, 253:110971.
- Rober, N., Mahesh, K., Paine, T. M., Greene, M. L., Lee, S., Monteiro, S. T., Benjamin, M. R., and How, J. P. (2024). Online data-driven safety certification for systems subject to unknown disturbances. In *Proc. IEEE Int. Conf. Robot. Autom.* IEEE.
- Rynne, P. F. and von Ellenrieder, K. D. (2009). Unmanned autonomous sailing: Current status and future role in sustained ocean observations. *Marine Tech. Soc. J.*, 43(1):21–30.

- Shen, Z., Wang, Y., Yu, H., and Guo, C. (2020). Finite-time adaptive tracking control of marine vehicles with complex unknowns and input saturation. *Ocean Eng.*, 198:106980.
- Sidrane, C., Maleki, A., Irfan, A., and Kochenderfer, M. J. (2022). OVERT: An algorithm for safety verification of neural network control policies for nonlinear systems. *J. Mach. Learn. Res.*, 23(117):1–45.
- Skejic, R., Breivik, M., Fossen, T. I., and Faltinsen, O. M. (2009). Modeling and control of underway replenishment operations in calm water. *Int. Fed. Autom. Control Proc. Vol.*, 42(18):78–85.
- Skjetne, R., Smogeli, Ø. N., and Fossen, T. I. (2004). A Nonlinear Ship Manoeuvering Model: Identification and adaptive control with experiments for a model ship. *Model.*, *Identif.*, *Control*, 25(1):3–27.
- Slotine, J.-J. E. and Li, W. (1987). On the adaptive control of robot manipulators. *Int. J. Robot. Res.*, 6(3):49–59.
- Smallwood, D. and Whitcomb, L. (2004). Model-based dynamic positioning of underwater robotic vehicles: Theory and experiment. *IEEE J. Ocean. Eng.*, 29(1):169–186.
- Tjeng, V., Xiao, K. Y., and Tedrake, R. (2017). Evaluating robustness of neural networks with mixed integer programming. In *Proc. Int. Conf. Learn. Represent*.
- Vincent, J. A. and Schwager, M. (2021). Reachable polyhedral marching (RPM): A safety verification algorithm for robotic systems with deep neural network components. In *Proc. IEEE Int. Conf. Robot. Autom.*, pages 9029–9035. IEEE.
- Weng, L., Zhang, H., Chen, H., Song, Z., Hsieh, C.-J., Daniel, L., Boning, D., and Dhillon, I. (2018). Towards fast computation of certified robustness for RELU networks. In *Proc. Int. Conf. Mach. Learn.*, pages 5276–5285. PMLR.
- Whitcomb, L. and Yoerger, D. (1996). Preliminary experiments in the model-based dynamic control of marine thrusters. In *Proc. IEEE Int. Conf. Robot. Autom.*, volume 3, pages 2166–2173.
- Woo, J., Park, J., Yu, C., and Kim, N. (2018). Dynamic model identification of unmanned surface vehicles using deep learning network. *Appl. Ocean Res.*, 78:123–133.
- Xiang, W., Tran, H.-D., Yang, X., and Johnson, T. T. (2020). Reachable set estimation for neural network control systems: A simulation-guided approach. *IEEE Trans. Neural Netw. Learn. Syst.*, 32(5):1821–1830.
- Xu, K., Shi, Z., Zhang, H., Wang, Y., Chang, K.-W., Huang, M., Kailkhura, B., Lin, X., and Hsieh, C.-J. (2020). Automatic perturbation analysis for scalable certified robustness and beyond. *Adv. Neural Inf. Proc. Syst.*, 33:1129–1141.
- Yoerger, D. and Slotine, J.-J. (1991). Adaptive sliding control of an experimental underwater vehicle. In *Proc. IEEE Int. Conf. Robot. Autom.*, volume 3, pages 2746–2751.
- Yuh, J., Marani, G., and Blidberg, D. R. (2011). Applications of marine robotic vehicles. *Intell. Serv. Robot.*, 4:221–231.
- Zereik, E., Bibuli, M., Mišković, N., Ridao, P., and Pascoal, A. (2018). Challenges and future trends in marine robotics. *Annu. Rev. Control*, 46:350–368.
- Zhang, H., Weng, T.-W., Chen, P.-Y., Hsieh, C.-J., and Daniel, L. (2008). Efficient neural network robustness certification with general activation functions. In *Adv. Neural Inf. Process. Syst.*, volume 31.
- Zhou, J., Ren, J., and Bai, W. (2023). Survey on hydrodynamic analysis of ship–ship interaction during the past decade. *Ocean Eng.*, 278.

Appendices

A Block diagram of controller architecture

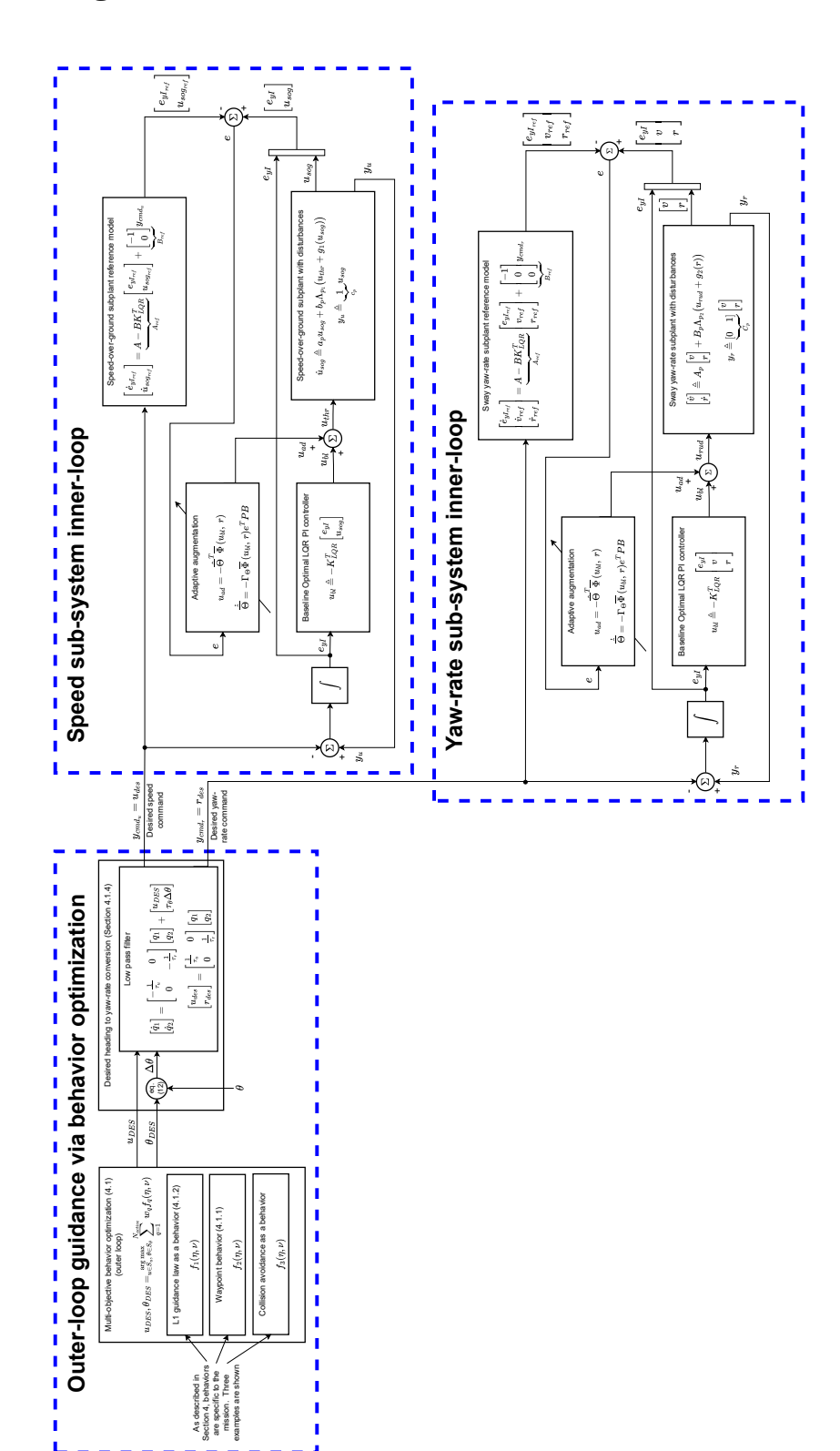


Figure 22: Block diagram of MRAC architecture.

B Block diagram of forward reachability analysis method

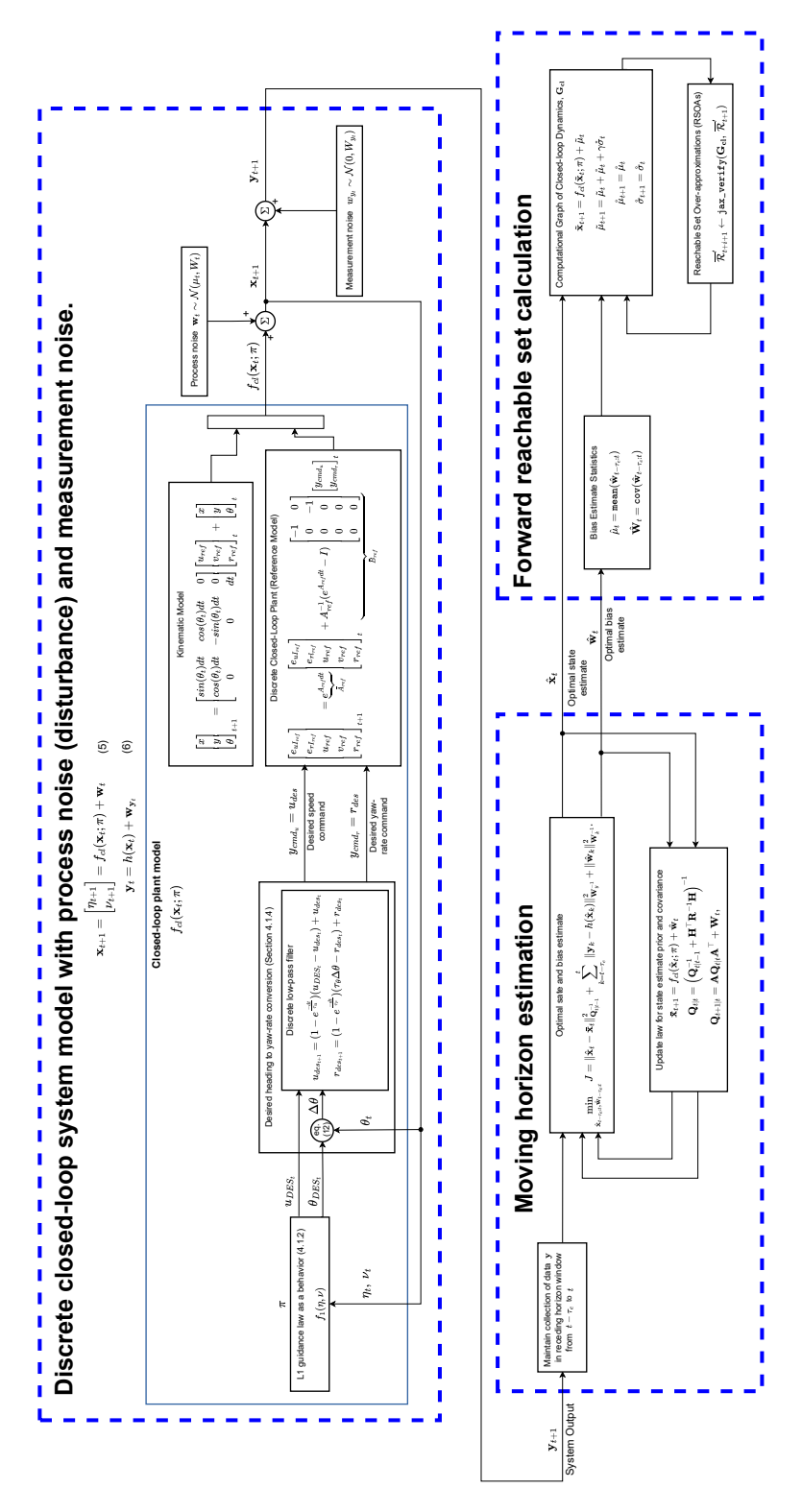


Figure 23: Block diagram of real-time forward reachability analysis with moving horizon estimation.